

Overview of C-2W: high temperature, steady-state beam-driven field-reversed configuration plasmas

H. Gota^{1,*}, M.W. Binderbauer¹, T. Tajima^{1,3}, A. Smirnov¹, S. Putvinski¹, M. Tuszewski¹, S.A. Dettrick¹, D.K. Gupta¹, S. Korepanov¹, R.M. Magee¹, J. Park¹, T. Roche¹, J.A. Romero¹, E. Trask¹, X. Yang¹, P. Yushmanov¹, K. Zhai¹, T. DeHaas¹, M.E. Griswold¹, S. Gupta¹, S. Abramov¹, A. Alexander¹, I. Allfrey¹, R. Andow¹, B. Barnett¹, M. Beall¹, N.G. Bolte¹, E. Bomgardner¹, A. Bondarenko¹, F. Ceccherini¹, L. Chao¹, R. Clary¹, A. Cooper¹, C. Deng¹, A. Dunaevsky¹, P. Feng¹, C. Finucane¹, D. Fluegge¹, L. Galeotti¹, S. Galkin¹, K. Galvin¹, E.M. Granstedt¹, K. Hubbard¹, I. Isakov¹, M. Kaur^{1,3}, J.S. Kinley¹, A. Korepanov¹, S. Krause¹, C.K. Lau¹, A. Lednev¹, H. Leinweber¹, J. Leuenberger¹, D. Lieurance¹, D. Madura¹, J. Margo¹, D. Marshall¹, R. Marshall¹, T. Matsumoto^{1,3}, V. Matvienko¹, M. Meekins¹, W. Melian¹, R. Mendoza¹, R. Michel¹, Y. Mok¹, M. Morehouse¹, R. Morris¹, L. Morton¹, M. Nations¹, A. Necas¹, S. Nicks¹, G. Nwoke¹, M. Onofri¹, A. Ottaviano¹, R. Page¹, E. Parke¹, K. Phung¹, G. Player^{1,3}, I. Sato¹, T.M. Schindler¹, J.H. Schroeder¹, D. Sheftman¹, A. Sibley¹, A. Siddiq¹, M. Signorelli¹, M. Slepchenkov¹, R.J. Smith¹, G. Snitchler¹, V. Sokolov¹, Y. Song¹, L.C. Steinhauer¹, V. Stylianou¹, J. Sweeney¹, J.B. Titus¹, A. Tkachev^{1,3}, M. Tobin¹, J. Ufnal¹, T. Valentine¹, A.D. Van Drie¹, J. Ward¹, C. Weixel¹, C. White¹, M. Wollenberg¹, S. Ziaei¹, the TAE Team¹, L. Schmitz^{1,2}, Z. Lin³, A.A. Ivanov⁴, T. Asai⁵, E.A. Baltz⁶, M. Dikovskiy⁶, W.D. Heavlin⁶, S. Geraedts⁶, I. Langmore⁶, P.C. Norgaard⁶, R. Von Behren⁶, T. Madams⁶, A. Kast⁶ and J.C. Platt⁶

¹ TAE Technologies, Inc., Foothill Ranch, CA, United States of America

² University of California at Los Angeles, Los Angeles, CA, United States of America

³ University of California at Irvine, Irvine, CA, United States of America

⁴ Budker Institute of Nuclear Physics, Novosibirsk, Russia

⁵ Nihon University, Tokyo, Japan

⁶ Google LLC, Mountain View, CA, United States of America

E-mail: hgota@tae.com

Received 30 May 2021, revised 6 August 2021

Accepted for publication 9 September 2021

Published 8 October 2021



Abstract

TAE Technologies, Inc. (TAE) is pursuing an alternative approach to magnetically confined fusion, which relies on field-reversed configuration (FRC) plasmas composed of mostly energetic and well-confined particles by means of a state-of-the-art tunable energy neutral-beam (NB) injector system. TAE's current experimental device, C-2W (also called 'Norman'), is the world's largest compact-toroid device and has made significant progress in FRC performance, producing record breaking, high temperature (electron temperature,

* Author to whom any correspondence should be addressed.

$T_e > 500$ eV; total electron and ion temperature, $T_{\text{tot}} > 3$ keV) advanced beam-driven FRC plasmas, dominated by injected fast particles and sustained in steady-state for up to 30 ms, which is limited by NB pulse duration. C-2W produces significantly better FRC performance than the preceding C-2U experiment, in part due to Google's machine-learning framework for experimental optimization, which has contributed to the discovery of a new operational regime where novel settings for the formation section and the confinement region yield consistently reproducible, hot, and stable plasmas. An active plasma control system has been developed and utilized in C-2W to produce consistent FRC performance as well as for reliable machine operations using magnets, electrodes, gas injection, and tunable NBs. The active control system has demonstrated stabilization of FRC axial instability. Overall FRC performance is well correlated with NBs and edge-biasing system, where higher total plasma energy is obtained by increasing both NB injection power and applied-voltage on biasing electrodes. C-2W divertors have demonstrated a good electron heat confinement on open-field-lines using strong magnetic mirror fields as well as expanding the magnetic field in the divertors (expansion ratio > 30); the energy lost per electron ion pair, $\eta_e \sim 6-8$, is achieved, which is close to the ideal theoretical minimum.

Keywords: field-reversed configuration, compact toroid, neutral-beam injection, edge biasing, active plasma control, steady state, aneutronic fusion

(Some figures may appear in colour only in the online journal)

1. Introduction

TAE Technologies, Inc. (TAE; formerly named Tri Alpha Energy) was established in 1998 as a fusion start-up private company [1], located in Southern California, aiming for the development and steady operation of commercial fusion reactors, and is currently one of the world's largest privately-funded fusion research companies. TAE's concept of a magnetically-confined fusion reactor is based on utilizing a field-reversed configuration (FRC) [2, 3] as the core plasma and performing plasma heating and current drive for steady operation by neutral beam (NB) injection (NBI). While at other large fusion devices D-T fuel is mainly considered for use in fusion reactor development and for steady operation [4, 5], TAE's approach is to eventually adopt advanced fuels such as p-¹¹B (possibly D-³He as well) with the ultimate aim of a safe and economical fusion reactor that does not generate neutrons in its primary fusion reaction [6, 7]. This approach also has many technological advantages that make it easier to design, construct and operate the reactor because there is little to no concern about neutron induced damage on the reactor. However, the conditions for fusion reactions/burning plasmas are more difficult and challenging than those for D-T reactions. Therefore, achieving the fusion condition with the realization of steady-state operation is our key project at TAE.

An FRC is a high-beta compact toroid (CT), solely consisting of poloidal axisymmetric magnetic field inside closed-field lines formed by the toroidal self-current, where its separatrix is surrounded by open-field lines [2, 3]. The volume-averaged beta (ratio of plasma pressure to external magnetic pressure) is close to 100%, so FRCs can be compact and highly magnetically efficient thus economically attractive as a fusion reactor plasma. Furthermore, because the closed-magnetic-field line

structure exists independently of the open-magnetic-field lines outside the separatrix, FRCs can be easily translated in the axial direction. A direct energy conversion can also be utilized by using natural divertors at both ends of the device.

TAE's current experimental device, C-2W (also called 'Norman', shown in figure 1), is the company's fifth generation FRC device and the world's largest theta-pinch, CT collisional-merging system [8]. It forms high-magnetic-flux, high-temperature, stable and long-lived FRC plasmas. In the preceding FRC experiments, C-2 [9, 10] and C-2U [11, 12], the primary goals were to study aspects and demonstration of the FRC plasma sustainment by NBI and edge biasing, and their key results and accomplishments were as follows: robust FRC formation via CT collisional-merging technique [9, 13]; production of high-performance FRC (HPF) plasmas with drastically improved particle and energy confinement properties [10, 14]; rapid accumulation of injected fast ions where about half of the initial FRC thermal pressure was replaced by fast-ion pressure [10, 11]; FRC lifetime and global plasma stability scaled strongly with synergetic effect of NBI power and edge biasing, where under the optimum C-2U operating condition FRC was sustained for 5+ ms and its configuration lifetime extended up to 10 ms via ~ 10 MW NBI (note that the performance was mostly limited by hardware and stored energy constraints such as the NB's pulse duration of up to ~ 8 ms flat-top and the current sourcing capability of the edge-biasing system whose operating voltage and duration were limited up to ~ 3 kV and ~ 7 ms, respectively) [11, 12]. In the current C-2W device (figure 1) several key subsystems were upgraded from C-2U, such as: higher NBI power (up to ~ 20 MW) with a tunable beam energy capability (15–40 keV) during a plasma shot, where NB pulse duration has also been extended up to 30 ms [15]; upgraded edge-biasing electrode systems

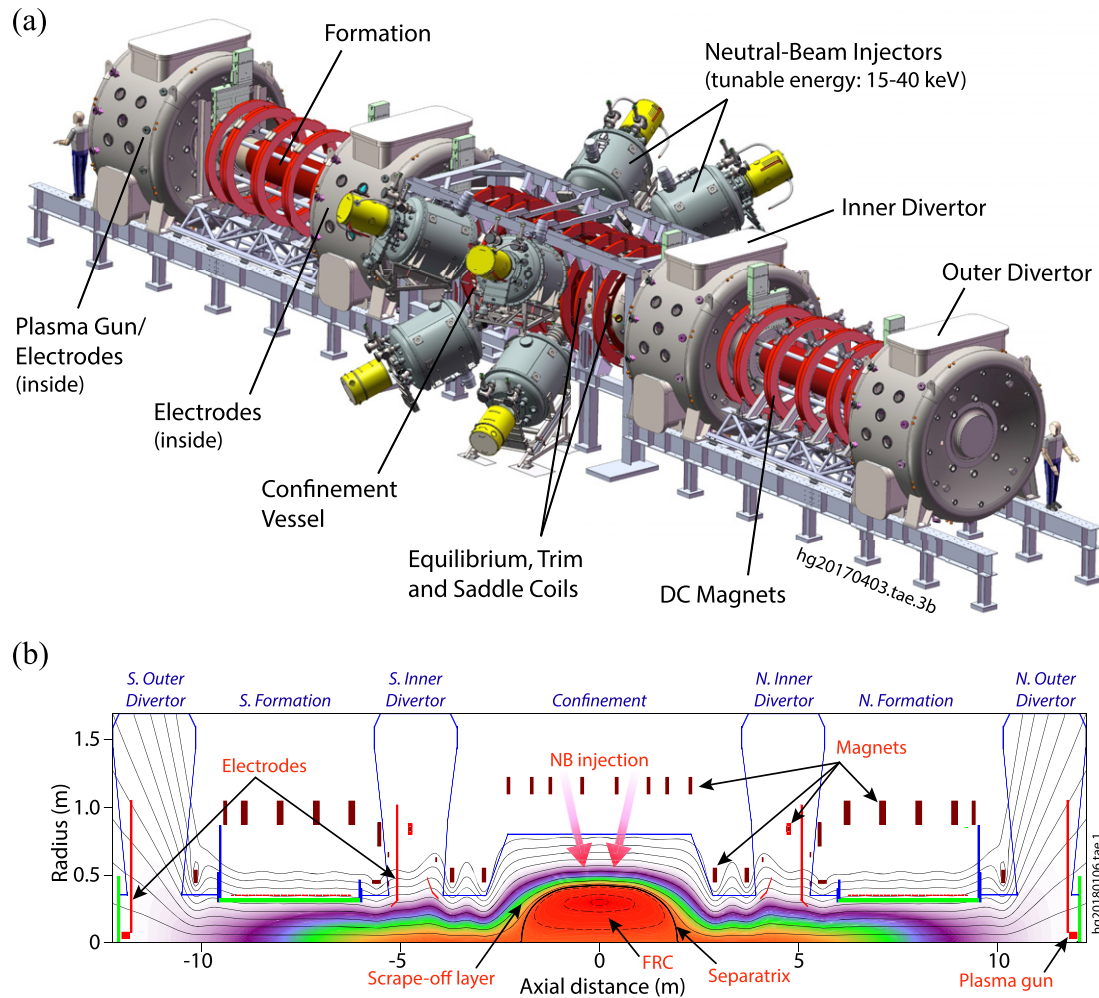


Figure 1. (a) Illustration of the C-2W experimental device, Norman, consisting of the central confinement section surrounded by 2 inner divertors, 2 formation sections, and 2 outer divertors. Eight NB injectors (4 of 15 keV fixed-energy NBs and 4 of 15–40 keV tunable-energy NBs) are installed in the central region of the confinement vessel. Plasma guns and electrodes are mounted inside divertors. (b) Sketch of FRC magnetic topology and density contours, calculated by 2D multifluid force-balanced equilibrium code [23], where field-line contours are traced and plasma densities are indicated with colors.

in both inner and outer divertors, allowing for higher biasing voltage (up to ~ 5 kV) and longer pulse operation (>30 ms) [16]; increased overall stored energy in the FRC formation pulsed-power system to produce better target FRCs for effective NBI heating and current drive; and fast external equilibrium/mirror-coil current ramp-up capability for plasma ramp-up and position/shape control, where additionally-installed trim/saddle coils can be used for active feedback plasma control [17]. C-2W has also enhanced overall diagnostic suite in both confinement and divertor regions to investigate and characterize core FRC plasma performance as well as open-field-line plasmas [18, 19]. In fact, as illustrated in figure 1(b), FRC plasma is surrounded by a large volume of open-field-line plasma that is confined by strong magnetic-mirror fields (so called ‘mirror’ plasma [20]). Therefore, understanding and improvement of open-field-line/mirror plasma characteristics are critical to the further advancement of core FRC plasma performance on C-2W.

Main goals of the C-2W experimental program are as follows: (a) demonstrate plasma ramp-up by NB heating and

current drive; (b) achieve high plasma temperature up to ~ 3 keV by improving edge and divertor plasma performance to increase high electron temperature both at the plasma edge and inside the core; (c) develop plasma control on the time scale significantly longer than L/R vessel-wall time and plasma confinement times, and demonstrate controllable plasma ramp-up; and (d) explore a wide range of plasma parameters such as plasma temperature, magnetic field and plasma size to confirm the previously obtained energy confinement scaling [12, 21]. As previously reported in reference [8], there were several key intermediate scientific and engineering milestones to accomplish and to accelerate the program towards the main goals, for instance: (i) producing a robust FRC formation and translation through inner divertors; (ii) establishing adequately controllable magnetic-field structure in the inner divertor area to change from guiding straight magnetic field for FRC translation to flared field structure, which enables edge biasing from the inner divertor region; (iii) demonstrating first of the kind active-feedback plasma control on FRC experiments; (iv) demonstrating sufficient particle refueling for

density control and plasma ramp-up; and, (v) establishing effective wall conditioning in the confinement vessel (CV) and high vacuum/pumping capability in all four divertors to reduce outgassing and secondary electron emissions (SEEs) from vessel-wall surfaces, thus improving open-field-line plasma conditions.

The present paper is organized as follows. Section 2 describes C-2W experimental apparatus, plasma diagnostic suite, advanced optometrist algorithm [22] for plasma optimization, and active plasma control systems. Key highlights and accomplishments of recent C-2W experiments are described in section 3, including characteristics of plasma stability and high-temperature regime. Lastly, a summary is provided in section 4.

2. C-2W experiments and operations

2.1. C-2W experimental apparatus overview

2.1.1. C-2W machine and vacuum vessel. The C-2W experimental device, shown in figure 1(a), is the world's largest theta-pinch CT collisional-merging system, utilizing high-power NBI and edge-biasing systems to form and sustain FRC plasmas. Figure 1(b) illustrates typical FRC magnetic flux and density contours in C-2W, obtained from a 2D multifluid force-balanced equilibrium calculation using LReqMI code [23]. The C-2W device has ~ 30 m in overall length and consists of the central confinement section surrounded by 2 inner divertors, 2 field-reversed theta-pinch (FRTP) formation sections, and 2 outer divertors, where those 7 sections can be independently isolated in terms of their vacuum boundary by large gate valves. The CV is made of Inconel and has an inner-wall radius $r_w \sim 0.8$ m with a thin wall whose resistive wall time is about 2–3 ms, which allows for magnetic-field ramp-up as required during a plasma discharge. Because of the relatively short wall time of the CV, adequately controlled external magnetic field is important and critical to FRC plasma confinement as well as for plasma ramp-up. The divertor vessels are made of stainless steel and have a large internal volume (~ 15 m³ per divertor) to accommodate a high volumetric pumping during a plasma discharge. Furthermore, each divertor has its own internal cryogenic pumping system with titanium gettering and liquid-nitrogen cooling system in place to enhance pumping capability inside divertors, where the pumping speed is ~ 2000 m³ s⁻¹ per divertor. The formation tubes are made of quartz, which are approximately ~ 3.5 m in length and ~ 0.6 m in diameter. The overall C-2W device accommodates an ultra-high vacuum (typical vacuum level is at in the range of high 10^{-10} to low 10^{-9} Torr) with adequately set up wall conditioning and pumping systems.

2.1.2. Magnet systems. C-2W magnets consist of confinement equilibrium and mirror coils, saddle and trim coils, in-vacuum fast-switching coils, DC formation/divertor coils, and magnetic-mirror plug coils, where the overall coil configuration is symmetrically arranged relative to the machine mid-plane ($z = 0$). A simple layout of the magnet systems in the confinement section is shown in figure 2. In the formation

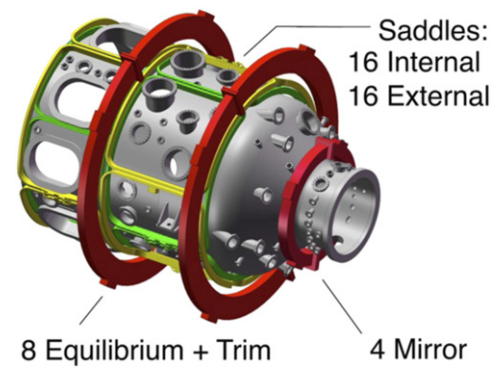


Figure 2. A layout of magnets (equilibrium, mirror, trim and saddle coils) in the C-2W confinement section for plasma confinement as well as for active plasma controls. A half of the CV is shown for simplicity.

section there are also 17 sets of pulsed-power formation coils located just outside of the quartz tube. Current waveforms of each equilibrium and mirror coils are independently controlled, which allows for an adequate and flexible control of external magnetic field profile as well as plasma shape and position. In the typical C-2W experiment, external axial magnetic field, B_z , in the confinement section is about 0.1 T and can be ramped up to ~ 0.3 T, at which confinement mirror field is also ramped up accordingly to confine FRC plasma within the mirror regions. Trim coils are placed beneath each of the equilibrium coils that can also be operated independently to correct error fields as well as to perform active feedback control. Saddle coils are deployed non-axisymmetrically around the CV and can be operated either passively with a shorted-coil configuration or actively with their power supplies for plasma position control. In-vacuum fast-switching coils are mounted inside the inner divertors to provide adequate guide magnetic fields during FRC translation as well as to quickly flare the fields by reversing the coil current within a few milliseconds. Magnetic mirror plugs are placed in between the formation and outer divertor sections at each side that can produce a strong magnetic field up to ~ 1 T. Together with the magnetic mirror plugs, outer divertor magnets also play an important role in controlling field expansion in the divertor regions.

2.1.3. Pulsed-power systems. An initial FRC plasma is generated by dynamic FRTP formation technique with pulsed-power systems in the formation sections [8, 9]. There are 17 sets of independently-controlled and energized formation-coil straps in each formation section, where the pulsed-power systems consist of Bias modules for negative-bias magnetic field ($B_z \sim -0.1$ T), main-reversal (MR) modules for main theta-pinch magnetic field ($B_z \sim 0.3$ – 0.4 T; risetime ~ 4 μ s), and rotating magnetic field (RMF) modules for deuterium gas pre-ionization inside the formation quartz tube. Note that we define ' $t = 0$ ' in our FRC experiments as the time when the 1st MR module gets discharged/triggered, and subsequently triggered other MR modules to form FRC plasma dynamically. Those modules have been substantially upgraded in C-2W, where the stored energies of each system increased

significantly (total stored energy > 2 MJ at typical operating condition) as well as system reliability and operating performance have improved considerably. In order to maintain the pulsed-power system reliability/performance as well as to detect/identify any system failure during a discharge, an automated signal classification system using a machine-learning algorithm (multi-layered neural network) has been developed and implemented in C-2W [24]. Due to such an improved overall pulsed-power system performance, the FRC plasmas generated in each formation section contain more magnetic and kinetic energies, which results in higher thermal energy after the initial FRC collision and merging in the confinement section. As previously reported in reference [8], very robust FRC formation and translation have been obtained in C-2W, where two FRCs collide with the relative speed of up to ~ 1000 km s^{-1} and merge into a single FRC that initial merged state exhibited a high plasma temperature condition: electron temperature of ~ 250 eV and total temperature exceeding 1.5 keV.

2.1.4. Neutral beams. Eight NB injectors are installed in the central region of the CV, 4 of which have a tunable beam energy (15–40 keV) capability [15] and the other 4 injectors have a fixed beam energy at 15 keV [25]. Total NB input (electrical) power with all 15 keV NBs is ~ 13 MW and can be increased up to ~ 20 MW by ramping beam energies, where its pulse duration is up to 30 ms. Nominal ion current per source is ~ 130 A (for both fixed and tunable energy NBs), and NB focal length and divergence are ~ 3.5 m and ~ 0.04 rad, respectively. NBI angle is presently fixed at 70° relative to the machine axis but can be changed in the range of 65° – 75° . Average NBI impact parameter (co-current injection) is ~ 20 cm that enables sufficient coupling between the beams and the target FRC plasma (typical radius of ~ 40 – 45 cm). NBs are typically operated with hydrogen but can be fueled with deuterium for a diagnostic purpose. Figure 3 illustrates a calculated 15 keV proton/hydrogen orbit in the C-2W midplane with plasma radius (r_s) of 40 cm and external magnetic field at the vessel wall (B_w) of 0.1 T. The NBs provide energetic particles with a large orbit size crossing inside and outside of the FRC separatrix that stabilize global magnetohydro-dynamic (MHD) modes [14]. They also provide a significant amount of fast-ion population and pressure inside the core, therefore producing beam-driven FRC plasma state. During the plasma pressure build-up via ramping up NBI power, the external magnetic field in the CV also needs to be increased to maintain the plasma radius, accordingly.

2.1.5. Edge-biasing systems. In order to control open-field-line plasmas and to provide sufficient radial electric field for $E \times B$ shearing around the FRC separatrix, GDT-type coaxial plasma guns [20] and concentric annular electrodes [16] are installed inside of each outer divertor as shown in figure 1(b). Figure 4 illustrates a simple sketch of edge-biasing current propagation from end electrodes to FRC core and scrape-off layer (SOL) region through open-field lines. Negatively-biased central electrodes and plasma guns create an inward radial electric field ($E_r < 0$) that propagates to the SOL region and produces azimuthal flow (flow speed $v_\theta \sim E_r \times B_z$) just

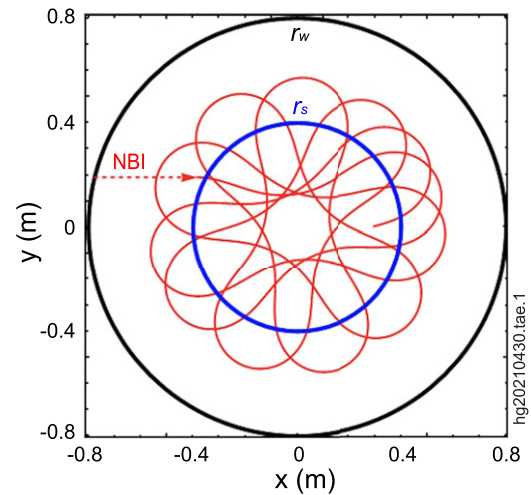


Figure 3. Calculated 15 keV proton/hydrogen orbit in the midplane of C-2W FRC. Dashed line/arrow indicates the direction of NBI, and solid line is the trajectory of the born fast ion that travels inside and outside of FRC separatrix r_s .

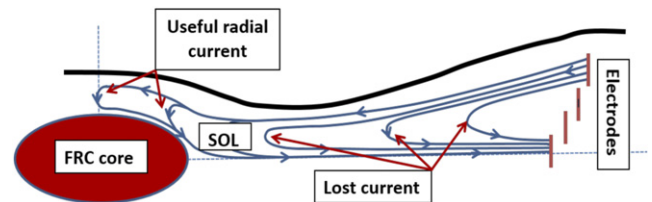


Figure 4. A sketch of biasing current propagation from end electrodes to FRC core and SOL region through open-field lines as well as returning back to the central electrode. To maintain the biasing current, gas-fueling system is utilized with feedforward and feedback controls in C-2W.

outside of FRC separatrix. It counters the usual FRC spin-up in the ion diamagnetic direction and suppresses $n = 2$ rotational instability (n : toroidal mode number). Better plasma centering (less $n = 1$ wobble motion) is also obtained from line-tying to the end electrodes and plasma guns, therefore NBs can be injected more efficiently into near-axisymmetric FRC discharges, which improves beam trapping and fast-ion confinement inside the FRC [14]. The edge-biasing electrode system has a good flexibility in terms of its operations, for instance relatively high voltage (up to ~ 5 kV) can be applied on the electrodes and its pulse duration is longer than 30 ms. In addition, similarly developed annular electrodes (with a hole in the central electrode, required for FRC translation) are installed in the inner divertors. Electrical potentials on those electrodes can be controlled independently by their power supplies, where an active voltage and current control has been implemented to control and maintain reliable edge-biasing current. This is the key element of reliable C-2W operations, together with magnetic field control in the CV and divertor regions, for effective edge/boundary control of FRCs via open-field-lines and SOL. The role of SOL and divertors is not only to provide a favorable boundary condition for the core FRC plasma but also to handle energy and particle exhaust from the core.

Table 1. C-2W diagnostic suite on FRC and open-field-line plasmas.

Shape / Position	Temperature / Density	Fluctuations / Radiation	Fast ions / Neutrals
Linear B-probe arrays	FIR interferometer	Mirnov probe arrays	Proton detectors
Linear Φ -loop arrays	Thomson scattering	DBS/CPS reflectometer	Neutron detectors
Fast-framing cameras	μ -wave interferometer	Azimuthal bolometer array	Fast-ion D_α spectrometer
Linear bolometer array	mm-wave interferometer	Survey spectrometers	SEE detectors
FIR polarimeter	Langmuir probes	End-on bolometers	Neutral particle analyzers
Dispersion interferometer	Impurity-ion ChERS	VUV spectrometer	Diagnostic neutral beam
Internal Rogowski coils	Main-ion ChERS	D_α fan arrays	Fast-ionization gauges
Internal B-probe array	Heterodyne spectrometer	Bremsstrahlung fan arrays	NB calorimeters
	End-loss energy analyzers		Thermo-optical arrays
			Pyro bolometers

2.1.6. Particle-fueling systems. Plasma particle inventory (amount of fuel) must be controlled to maintain proper densities for NB capture, which is required in the presence of particle losses from the core that is unavoidable. A plasma refueling system must be capable of matching the particle losses as well as increasing the total particle inventory if desired. Azimuthal current in FRC flows across magnetic field lines, thus maintaining total pressure gradient in the core is essential for the sustainment of magnetic flux of FRC and its configuration. Without central refueling and heating the trapped magnetic flux decays due to finite plasma resistivity across magnetic field. To that end, there are mainly three particle refueling systems currently deployed on C-2W: multi-pulsed CT (spheromak-like plasmoid) injector systems near the midplane [26, 27], cryogenic pellet injector system [28], and gas injection systems at various locations throughout the machine. The CT and pellet injectors are primarily used for particle refueling in the core region, while the gas injection system is mainly used for edge density control in the SOL and open-field-line region that allows sufficient edge-biasing current to maintain for FRC plasma stabilization (figure 4). The CT injector can produce and inject $\sim 10^{19}$ particles per pulse (up to 10 pulses from 2 CT injectors) at the speed of up to $\sim 100 \text{ km s}^{-1}$ into the CV and FRC, while the pellet injector can introduce $0.5\text{--}1.0 \times 10^{19}$ particles per pellet at the speed of $0.2\text{--}0.5 \text{ km s}^{-1}$. The gas injection system can be operated with various operating conditions such as single gas puff (e.g. for formation sections), continuous gas flow, and modulated or instant gas fueling using either pre-programmed/feedforward or active/feedback control systems.

2.2. Plasma diagnostic suite

The C-2W experimental device currently has 62 operational out of 72 planned diagnostic systems deployed and collecting data [18, 19]. The diagnostics are spread out over the entirety of the machine with good coverage throughout the CV, inner/outer divertors, and formation sections. The diagnostic suite's purpose is to measure the behavior of FRC/open-field-line plasmas throughout the machine. In previous machines at TAE primary focus was on the FRC core of the plasma, particularly at the midplane of the device. In C-2W the role of the open-field-line plasma has proven to be nearly as important at the core behavior. The open-field-line plasma

plays a significant role in stabilizing and controlling the core plasma. As such, the distribution of measurement capability is far more widespread throughout the device, but the main focus is still on the core region. Table 1 contains a list of the various diagnostic systems which are deployed on C-2W. They are grouped according to their primary function. The diagnostics deployed on C-2W are required to provide data for a very wide range of plasma parameters to follow the discharge evolution from a seed FRC to a much hotter and higher energy state. Plasma performance and various other parameters are discerned using this comprehensive suite of diagnostics that includes: a variety of magnetic probes [29]; several iterations of bolometers; multiple interferometers including a far-infrared (FIR) interferometer/polarimeter [30], millimeter-wave interferometer [31], dispersion interferometer [32], and micrometer-wave interferometer [33]; core and jet region Thomson scattering systems [34, 35]; spectroscopy of many varieties including impurity- and main-ion charge-exchange recombination spectroscopy (ChERS) [36, 37], a combination doppler backscattering/cross-polarization scattering reflectometer [38], fast-ion D_α spectrometer [39], VUV spectrometer, and survey spectrometers; multiple fast-imaging cameras [40], He-jet imaging cameras [41]; bremsstrahlung/ D_α fan arrays [42]; beam calorimeters [43]; secondary electron emission (SEE) detectors [44]; thermo-optical sensor arrays; various Langmuir probes [45, 46]; end-loss energy analyzers [47]; fast ionization gauges; diagnostic neutral beam; neutron detectors [48]; neutral particle analyzers [49]; and proton detectors [50]. Signals and data from each of the diagnostic systems are transferred to a data-acquisition system that acquires several 1000s channels on every C-2W discharge. The raw data are post-processed into plasma parameters and then stored in a physics database for further data analysis. Some raw data, such as magnetic probe signals, get processed continuously during a plasma discharge through the real-time control system for use in active feedback control of the plasma [17]. Each C-2W shot generates more than 5 gigabytes of data, including analysis movies and computations; data usage was greatly reduced by employing single-precision floating point in the final product for processed signals, while continuing to save raw signals with high precision. More detailed descriptions of the diagnostics suite and some of its direct applications can be found in references [18, 19].

2.3. Advanced optometrist algorithm

To optimize the performance of the C-2W device and plasma parameters, the previously developed optometrist algorithm with Google for use in C-2U experiments [22] has been expanded. The primary advantage of the optometrist algorithm is combining the best of machine and human; the human provides physics intuition from experiments, while the machine searches high-dimensional parameter space. Rather than attempting to specify a figure of merit, the human expert makes a judgment call. They can use any data for a particular shot, including things as simple as total energy or maximum electron temperature, or as complex as the time evolution of density profiles or edge-biasing current, or even the presence of plasma perturbations. Whether a plasma shot is deemed to be ‘better’ or ‘worse’ than its reference can even depend on the particular goals of an experiment campaign. Although C-2W has thousands of configurable parameters, most subsystems can be effectively described by a much smaller space of meta-parameters (MPs), where we can adjust the effects of most subsystems with 1–2 MPs, capturing the most important behaviors. The optometrist algorithm is especially effective where human physics intuition fails. Typically, physical intuition is used to manually adjust 1–2 parameters at a time to get reasonable results. At this point the optometrist algorithm can take over a high-dimensional search to fine-tune the machine settings to achieve optimal performance.

Here, as an example, optimization of the FRTP FRC formation section is described. We included two significant advancements, involving control parameters and shot history. On the control side, the idea of MPs was expanded to include time dependence. Formation power supplies can supply pre-specified time-dependent current, where these waveforms can be described in a small number of parameters to be optimized. In addition, pulsed-power trigger/discharge timings (on the order of 10s of nanoseconds) turned out to be crucial. The C-2W formation sections have 17 sets of coil straps each side, to be fired in sequence to initiate, ionize, and accelerate the plasma, so called dynamic FRC formation and translation [8, 9]. Figure 5 shows an example of trigger timings of those formation coil straps (coil #0–16). Starting from a simple linear timing ramp (dotted lines in figure 5), these time sequences are parameterized in 4 linear segments with arbitrary positive slope. Applying the optometrist algorithm over three experimental-run days revealed an optimal pattern of 2%–3% deviations from a strictly linear timing ramp, as shown by solid lines in figure 5. Following this experiment, after one day of human-based manual optimizations on other subsystems such as magnets, gas injection and edge biasing systems, the pulsed-power settings derived by the optometrist algorithm were also applied; at which, on the second plasma shot, breakthrough performance of FRC was achieved as plasma lifetime extended by 200%–300%. This newly-emerged and optimized regime rapidly led to present plasmas with ~ 30 ms lifetime (see figure 9 for instance). For the sake of detailed discussion and specifics of the optimization process and technique during the FRC performance breakthrough period, we consider a separate and dedicated report elsewhere in the future. Instead, in

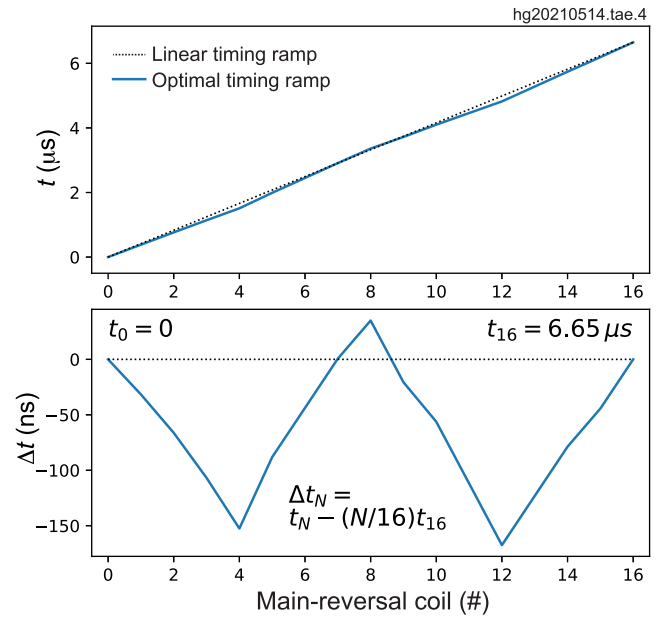


Figure 5. Trigger timings of 17 FRTP formation coil straps (for main reversal) for linear timing ramp (dotted lines) and optimized timing ramp (solid lines), where Δt is the time difference between the two ramp timings.

this section we present only some specific examples of C-2W optimization experiments using the optometrist algorithm.

Originally, the optometrist algorithm did not consider the history of results beyond comparing the reference experiment with the current experiment. The new algorithm recently expanded on this by considering an arbitrary number of previous shots. Treating each experiment as a direction in MP space with a binary ‘better or worse’ result, a logistic regression is fitted. This is a standard technique in the family of generalized linear models [51] when the dependent variable is Boolean. The log-odds $\ln[P/(1 - P)]$ is modeled as a linear function of the independent variables. Fitting this regression gives the direction in MP space that is most favored by the human experimenter. The linear prediction of log-odds for an experiment is then just the dot product of the MP direction for the experiment with the linear fit direction. We take this one step further by fitting a second model with a limited set of quadratic terms. The features are simply the linear prediction itself, as well as the quadratic terms involving the linear prediction multiplying each of the original MP features in turn. In fitting this model, two basic scenarios are possible. If the optimization has not converged, the linear fit should remain viable. In ideal conditions the coefficient of the linear prediction itself should be 1, while the quadratic terms should be disfavored. If convergence to an optimum has been achieved, the linear prediction should be disfavored relative to the quadratic terms, and its coefficient should become small. The best fit direction is then used to bias the proposal directions in MP space, allowing for exploration but exploiting what has already been learned. This newly advanced optometrist algorithm with logistic regression (OALR) is now routinely used in C-2W experiments to optimize machine parameters and FRC performance.

As an example of the OALR in C-2W, figure 6 shows a one particular experimental run (a course of 28 shots, including a reference shot in the beginning) and its outcome. The profile and timing of the magnetic fields in the confinement mirror regions are adjusted, but leaving other machine settings unchanged. The basic strategy of this particular run is to optimize electron temperature of FRC core without reducing action (time integral of FRC thermal energy), though other criteria are also considered for each plasma shot by the human experimenter to judge ‘better’ or ‘worse’ performance (i.e. accept or reject the shot just taken). The optimization run succeeded in more than doubling the electron temperature while keeping the action level almost the same as in the initial reference shot. The linear fit quality can be expressed as an effective number of steps taken: simply the cumulative sum of the coefficients of the linear predictions at each step. In practice these coefficients are >0.5 when the model is converging, and drop to <0.1 when no further linear improvement is occurring. In this run four dimensions are being explored so there is no linear fit until five shots have been taken. The linear fit is reasonable for a number of shots, shown by the increasing cumulative number of linear steps. After about 20 shots the linear fit becomes strongly disfavored, shown by the plateau in the cumulative effective linear steps taken; this plateau indicates convergence. Following convergence, a new OALR experimental run with different variables can be explored to continue machine and parameter optimizations.

2.4. Active feedback plasma control systems

Keeping FRC plasma well centered inside the CV to minimize stochastic fast-ion losses is one of the key ingredients of the high-performance operating regime in C-2W. This can be achieved by a combination of edge biasing and magnetic control, and C-2W has the capability to control the behavior of the plasma in real-time [17]. By reading and interpreting plasma diagnostics during a shot, the feedback system is capable of affecting the length, shape, location, density, and overall stability of the plasma by changing various magnet currents, controlling edge-biasing electrode currents, varying tunable NB energy, and modifying gas fueling rates. The C-2W plasma control system provides high bandwidth (2.5 MHz) data acquisition and low latency (100 kHz/10 μ s) magnetic control of plasma shape and position as well as kinetic controls of electrode current, NBI grid acceleration voltage, and gas-puff valves at various location. Figure 7 shows simple schematics of plasma control system, where diagnostic measurements are interpreted in real-time and, based on control inputs, actuators are manipulated to generate the desired plasma response. The plasma control system is a distributed digital control system based on Speedgoat modules for fast data acquisition and plasma control, which use multi-gigabit transceivers with Xilinx Aurora protocol to communicate among data acquisition systems, control modules and actuators. The core functionality, system setup, observers, and control algorithms are implemented using Matlab scripts, Simulink, and HDL coder workflow. This enables a quick and easy transition from model-based designs to FPGA hardware implementations.

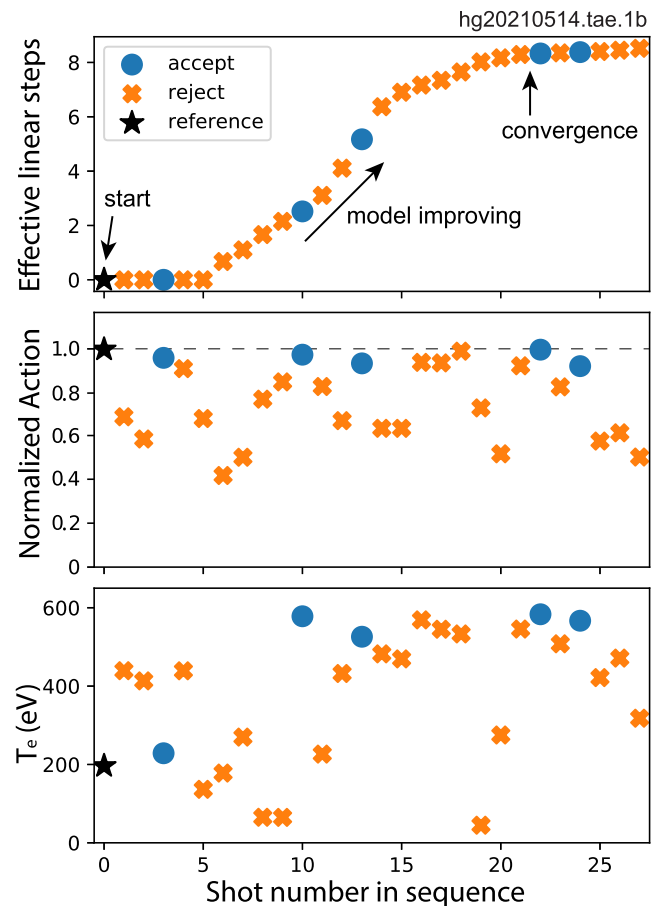


Figure 6. Example experimental run of optometrist algorithm with logistic regression. The main goal was to increase T_e (averaged spatially and temporally) without decreasing action (time integral of FRC thermal energy). The effective number of linear steps taken converges after about 20 shots.

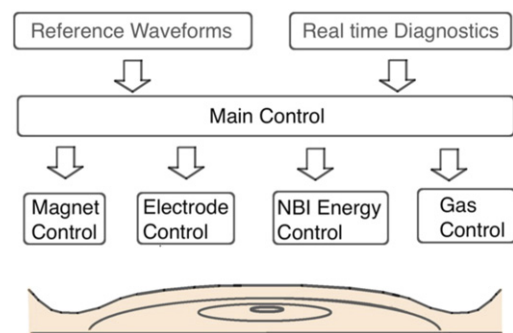


Figure 7. Schematics of the plasma control system. Control bandwidth is different for different subsystems, ranging from 500 Hz (gas injection system) to 20 kHz (Trim coils). Diagnostic measurements are interpreted in real-time and, based on control inputs, actuators are manipulated to generate the desired plasma response.

As an example of active plasma control on C-2W, the control system can mimic a perfect flux conserver and enhance the plasma performance or generate an axially unstable background field and use feedback to keep the plasma stabilized using various magnets (figure 2). By specifying a desired

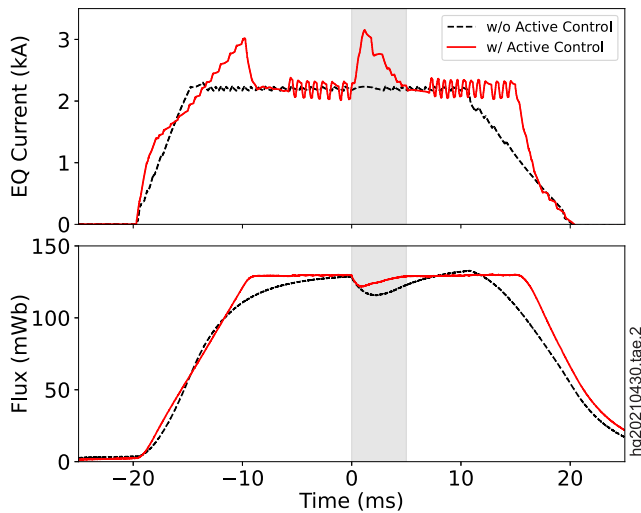


Figure 8. An example of active control on magnetic flux of the CV, serving as a flux conserver by regulating the equilibrium (EQ) current in real-time. Shaded area indicates the presence of FRC plasma inside the CV, where less flux leakage is observed with active control as compared to a shot without active control (i.e. constant EQ current, dashed line).

plasma condition before the shot, such as maintaining the total flux in the system (i.e. a perfect flux conserver), the control system will read several data streams during the shot and make adjustments to actuators (such as magnet currents) in real-time to achieve the desired flux function. A similar procedure can also be applied to a number of other plasma parameters as desired. Figure 8 shows an example of active magnetic-flux control, where equilibrium current is regulated in real-time to maintain the total amount of magnetic flux inside the CV wall. As compared with a case without active control (i.e. constant equilibrium field), more constant magnetic flux is observed throughout the discharge, in particular less flux leakage on the CV wall during the presence of FRC plasma (depicted as shaded area in the figure).

3. C-2W experimental results

As previously reported in reference [8], early C-2W experimental campaign was mostly devoted to explore and find optimum operating parameters and settings, particularly in the formation pulsed-power systems, gas fueling, magnetic-field profile throughout the machine, and edge-biasing systems using both outer and inner divertors. The early C-2W experiments went well to demonstrate a robust dynamic FRC formation and translation through inner divertors, and produced a much higher initial temperature state right after the CT's collisional merging, as compared to C-2U results [11, 12]. We then focused more on effective edge biasing and NBI on FRC plasma to stabilize it and extend its configuration lifetime. After a course of dedicated experimental campaign through various optimizations using Google's optometrist algorithm [22] and in-house active plasma control systems [17], C-2W has made significant progress in FRC performance (an

example shown in figure 9) and successfully achieved its program goals. This section describes characteristics of advanced beam-driven FRC plasmas as well as key recent accomplishments in C-2W.

3.1. Steady-state advanced beam-driven FRC

Producing a stable FRC for effective NBI is one of the most important elements to obtain a beam-driven FRC plasma state because the injected fast ions typically take ~ 1 ms to accumulate and develop sufficient pressure inside the FRC. Historically in the FRC research community, global plasma instability such as $n = 1$ and 2 modes (n : toroidal mode number) was a big issue to resolve and overcome in order to produce better FRC confinement as well as to prolong its configuration lifetime [2, 3]. However, in the preceding TAE's C-2 and C-2U experiments HPF and beam-driven FRC plasmas demonstrated a high degree of stabilization through the synergetic effect of edge biasing and NBI [10, 14, 52, 53], and finally achieved 5+ ms plasma sustainment as well as configuration lifetime of up to ~ 10 ms [11, 12]. In C-2W with significantly upgraded various subsystems, FRC performance has been further advanced but key ingredients to achieve such conditions are essentially the same as those in C-2/2U [10, 12]: (a) robust FRC formation via CT collisional merging; (b) effective vessel-wall conditioning and vacuum pumping; (c) effective edge biasing via end-on plasma guns and concentric annular electrodes; and (d) effective NBI into the target FRC for plasma heating and current drive.

As an example, figure 9 shows FRC performance comparison between C-2U (shot #43833 in red, also can be seen in figure 6 of reference [12] as one of the best-performed C-2U FRCs in terms of initial phase of plasma sustainment and its configuration lifetime, but not necessarily for total temperature or thermal energy) and early stage of C-2W experimental campaign, where C-2W shots (#113301 in blue and #114534 in green) clearly show the advancement of plasma parameters and also indicate hot and steady-state plasma discharges until the termination of NBI's; plasma parameters in the figure are the excluded-flux radius, averaged electron density, averaged electron temperature, total temperature, and thermal energy of FRCs. Several remarkable points in plasma performance of those C-2W shots are as follows: (a) building up significant plasma pressure after the initial dynamic phase of FRC collisional merging (e.g. $t > 3$ ms in shot 113 301), indicative of rapid accumulation of injected fast ions, at which the estimated trapped poloidal flux ϕ_p (based on rigid-rotor model [2, 54]) is also significantly increased (e.g. from ~ 4 mWb at 1 ms to ~ 10 mWb at 15 ms in shot 113 301); (b) FRC radius is well maintained by a controlled increase in the external magnetic field during the discharge (e.g. equilibrium field increased by $\sim 40\%$ over 30 ms for shot 114 534, and confinement mirror fields also increased to keep the axial profile of the magnetic field and to avoid FRC axial-shift instability); and (c) clearly increasing plasma temperatures (both T_e and T_{tot}) over time through NBI heating and possibly additional plasma heating via edge biasing (e.g. $E \times B$ heating) as well (T_{tot} in shot 114 534, for instance, is monotonically increasing after

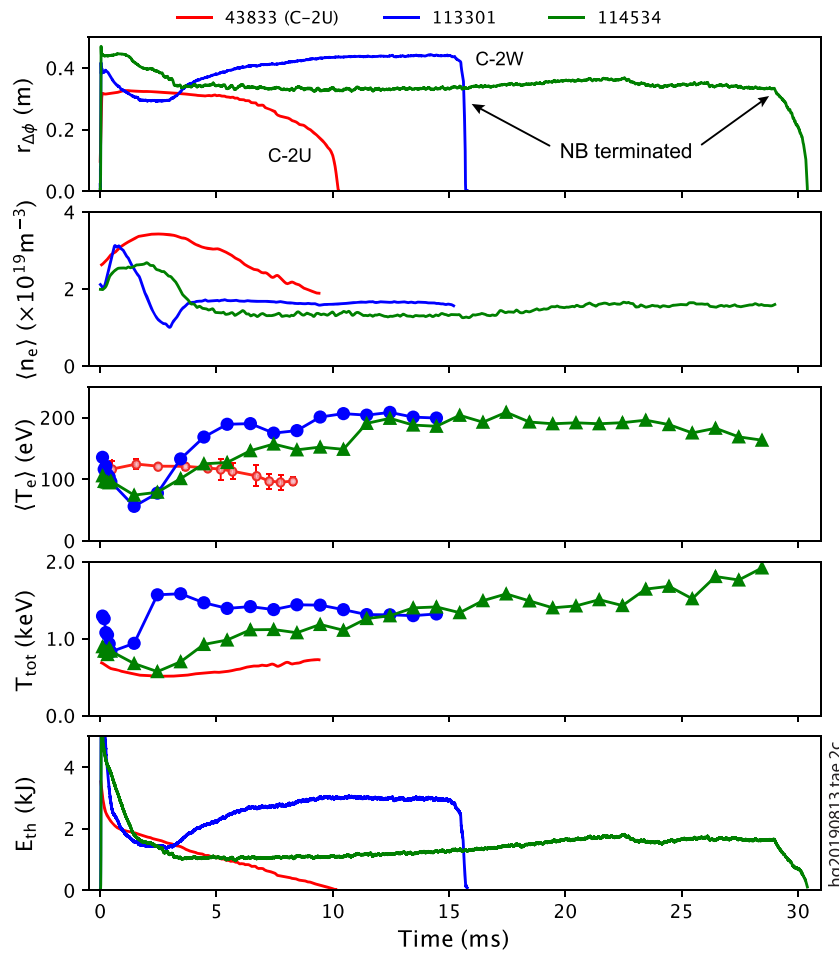


Figure 9. Time evolutions of excluded-flux radius $r_{\Delta\phi}$, averaged electron density n_e inside FRC radius measured by FIR interferometer, averaged electron temperature T_e inside FRC radius measured by Thomson scattering, total temperature T_{tot} estimated from pressure balance, and thermal energy E_{th} of FRCs for shots 113 301 (blue) and 114 534 (green) in C-2W, compared with shot 43 833 (red) in C-2U [12]. Note that C-2U Thomson scattering system had limited (up to 4) pulses per shot, therefore the data of C-2U T_e shown here is shot ensemble of similar operating condition to shot 43 833. Both C-2W shots are terminated due to the end of NBI.

~ 3 ms even though T_e and n_e stay relatively constant after at ~ 12 ms, appeared to be manifesting fast-ion effect such as building up fast-ion pressure, as discussed in section 3.3.2 later). Since the pulse duration of the C-2W NB system is limited up to 30 ms due to its power-supply energy storage, C-2W FRC has basically reached to the maximum and achievable pulse length of up to 30 ms as designed. Therefore, we then shifted and put more effort towards high-temperature plasma operations.

3.2. Characteristics of FRC stability and fluctuation

3.2.1. Magnetic fluctuation. A robust FRC formation and stable beam-driven FRC discharge are shown in figure 10. The initial collisional-merging FRC formation process occurs in the first few milliseconds and settles down to a stable regime, at which the density profile (Abel-inverted profile using the mid-plane multi-chord FIR interferometer) inside FRC develops a hollowness over time and its peak is located at just inside the excluded-flux radius of FRC ($r_{\Delta\phi}$: black solid lines). The hollow density profile is indicative of FRC structure [2], also well corroborated by fast-framing camera image with O 4+ optical

filter (semi-axial view from the end of the CV) [40] as shown in figure 11. The MHD magnetic fluctuation amplitude ($\delta B/B_z$) is determined using higher-order singular value decomposition (HOSVD) analysis of azimuthal arrays of 8 Mirnov probes located near the central region of the CV wall [29, 55]. Dominant patterns in the signal are identified by applying HOSVD to the data tensor. This process computes the strongest mode shapes in the azimuthal and axial dimensions simultaneously, while also describing their evolution in time. A small benign magnetic fluctuation can be seen in figure 10, where the dominant mode is $n = 1$ wobble motion and its amplitude $\delta B/B_z$ is below 0.005 (where $\delta B < 5 \times 10^{-4}$ T at $B_z \sim 0.1$ T). A benign fast-ion-driven microburst instability [56, 57] is also observed as seen in small wiggles of $n = 2$ mode after 25 ms. Note that relatively high fluctuation amplitude in the beginning of the discharge is due to the initial collisional-merging FRC formation process. More detailed mode analysis and discussion can be found in reference [55].

3.2.2. Density fluctuation. A four-channel Doppler backscattering (DBS) system is used in C-2W to investigate radial profiles and properties of turbulent density fluctuations [38].

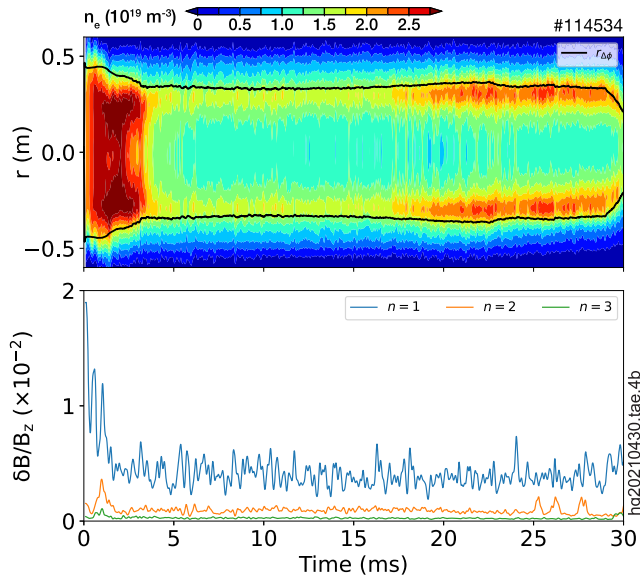


Figure 10. Time evolutions of Abel-inverted electron density profile from FIR interferometer with excluded-flux radius of FRC (top) and toroidal-mode ($n = 1-3$) magnetic fluctuation amplitudes measured by Mirnov probe arrays (bottom) for shot 114534.

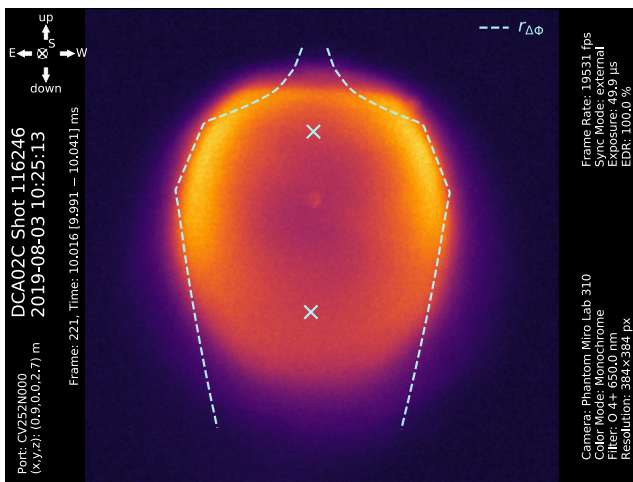


Figure 11. Fast-framing camera image (nearly axial view) of FRC plasma emission with O 4+ bandpass optical filter ($\lambda \sim 650.0 \pm 0.5 \text{ nm}$) at $t \sim 10 \text{ ms}$ of shot 116246. The view is from the top north end to the bottom south end of the CV (angled $\sim 18^\circ$ to the machine axis) [40]. Fitted excluded-flux radius profile with X-points (measurement of the FRC length) measured by magnetic probes is overlaid.

Due to the ability to control the incidence angle of the combined launched microwave beam (of width $\Delta W \leq 3 \text{ cm}$), the toroidal density fluctuation wavenumber spectrum $\tilde{n}(k_\theta)$ can be acquired from the amplitude of the backscattered signal. This information is in principle obtained simultaneously for four radial probing locations, and the probing radii are set by the launched DBS frequencies, tunable in between C-2W shots. Reconstruction of the plasma center (from FIR interferometry and spectroscopy) and the radial electron density profile from FIR interferometry is necessary to infer the DBS probing position and the probed density fluctuation wavenumber, based

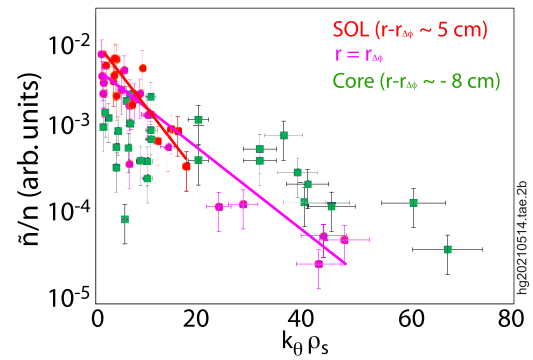


Figure 12. Toroidal wavenumber spectrum of density fluctuations measured by Doppler backscattering system inside (green), at (magenta), and outside (red) the excluded-flux radius of FRC ($r_{\Delta\phi}$).

on GENRAY ray tracing of the incident and backscattered microwave beam trajectories.

Figure 12 shows the measured dependence of the density fluctuation level on normalized toroidal wavenumber $k_\theta \rho_s$ in C-2W, for probing radii inside the FRC excluded-flux radius ($r_{\Delta\phi}$) as well as at/near $r_{\Delta\phi}$ and in the SOL plasma (i.e. outside $r_{\Delta\phi}$); where, $\rho_s = \sqrt{T_i/m_i}/\omega_{ci}$ is the ion sound gyro-radius. Typical estimated thermal ion Larmor radii are $\rho_i \sim 3 \text{ cm}$ for $r - r_{\Delta\phi} \sim 5 \text{ cm}$ (basically determined by the external magnetic field) and $\rho_i \sim 6 \text{ cm}$ for $r - r_{\Delta\phi} \sim -8 \text{ cm}$ (as inferred from FRC equilibrium reconstruction). This data demonstrates clearly that the density fluctuation wavenumber spectrum is near-exponential in the SOL and near $r_{\Delta\phi}$ as indicated by solid lines in the figure, but nearly flat inside $r_{\Delta\phi}$ in the outer region of FRC core plasma. The most transport-relevant fluctuations (at low normalized wavenumber) are significantly reduced in the FRC core as compared to the SOL, indicating that ion-scale turbulence is significantly lower in the FRC core compared to the surrounding SOL mirror plasma. These results are in qualitative agreement with earlier measurements in the C-2U FRC, where an inversion of the low- k wavenumber spectrum was observed in the FRC core [53]. Gyrokinetic calculations (with gyrokinetic ions and drift-kinetic electrons) attribute the observed core stability predominantly to the large thermal ion Larmor radius in the FRC core, and the short fieldline connection length in the FRC core [58].

3.2.3. Plasma rotation and velocity shear. Two dedicated ChERS diagnostics are routinely used to measure impurity-ion (e.g. oxygen 6+) as well as main-ion (deuterium) toroidal (or azimuthal) velocities, temperatures, and density profiles near the midplane of C-2W, where the newly-developed diagnostic NB is utilized for active measurements [36, 37]. The radial momentum balance equation for ions is given as

$$v_{\theta i} = v_{E \times B} + v_{Di} = -\frac{E_r}{B_z} + \frac{1}{eB_z Z_i n_i} \frac{\partial P_i}{\partial r}, \quad (1)$$

it provides an estimate of $E \times B$ velocity ($v_{E \times B}$) from the measured toroidal ion velocity ($v_{\theta i}$) and ion diamagnetic velocity (v_{Di}) for different ion species. A typical FRC is known to spin up in the ion diamagnetic direction, which may lead to $n = 2$ instability if the rotation parameter α (the ratio of

ion rotation to diamagnetic rotation) exceeds 1.2 [2]. In other words, $E \times B$ rotation adds to the diamagnetic rotation to speed up the FRC rotation, thus leading to a rotational instability such as elliptical distortion. In C-2W, however, externally-applied negative bias voltage on electrodes creates an inward radial electric field $-E_r$, thus $E \times B$ rotation in the electron diamagnetic direction which counters FRC's natural rotation. This slows down the plasma rotation and globally stabilizes the FRC [14].

As an example of the actual ChERS measurements, those three velocities in equation (1) near the FRC excluded-flux radius for different biasing voltages on electrodes are shown in figure 13. For negatively-applied bias voltage on electrodes (typically, negative potential applied to the central electrode with respect to the outer grounded electrode), the measured impurity-ion toroidal rotation is indeed in the electron diamagnetic direction, which is opposite to the ion diamagnetic direction. The $E \times B$ velocity is also in the electron diamagnetic direction, and it increases with higher negatively-applied bias voltage for edge biasing and stability control. The impurity-ion velocity, in the radial momentum equation (equation (1)), is dominated by the $E \times B$ velocity, and the contribution of impurity diamagnetic term is small. This is partly due to the $1/Z$ multiplier that significantly reduces the contribution of the diamagnetic term for higher charge-state impurity ions (such as O^{6+}). The impurity-ion velocity is nearly the same as the $E \times B$ velocity due to the small contribution of the diamagnetic term, which may also be taken as a proxy for the presence of a radial electric field (E_r) in the plasma with the applied bias voltage on electrodes. While on the contrary, the magnitude of diamagnetic velocity for main ions is significantly higher as compared to the impurity (oxygen) ions, partly due to a lower Z for deuterium ions. As shown in figure 13, the estimated main-ion velocity is small (near zero, or below 15 km s^{-1} at the excluded-flux radius of FRC), which is consistent with the direct measurement of main-ion velocity using an active spectroscopy with diagnostic NB [37]. Observations of the low main-ion rotation velocity and the $E \times B$ rotation direction support and validate our understanding of FRC stabilization via edge biasing.

The DBS system also provides an estimate for the $E \times B$ velocity based on the advection velocity of the probed turbulent structures. In the C-2W experiment, the $E \times B$ velocity (and the velocity shear) has been found to peak near the excluded-flux radius $r_{\Delta\phi}$, where the value is roughly proportional to the applied biasing voltage on electrodes, in the range of $v_{E \times B} \sim 5.5\text{--}7.5 \times 10^4 \text{ m s}^{-1}$ for applied biasing voltages $V_{\text{Bias}} \sim -1.8\text{--}2.3 \text{ kV}$. It is found that $v_{E \times B}$ and E_r decrease towards the plasma center and in the SOL. The measured $v_{E \times B}$ via DBS is consistent and agrees well with the $E \times B$ velocity measurement by the impurity-ion ChERS [36] near the FRC excluded-flux radius as shown in figure 13. The $E \times B$ velocity shearing rate, $\omega_{E \times B} = [v_{E \times B}(r_2) - v_{E \times B}(r_1)] / (r_2 - r_1) \leq 4.2 \times 10^5 \text{ rad s}^{-1}$, is comparable to the laboratory frame turbulence decorrelation rate, a criterion that needs to be satisfied for a significant reduction of turbulence via shear decorrelation [59]. In C-2W, this criterion is marginally satisfied near

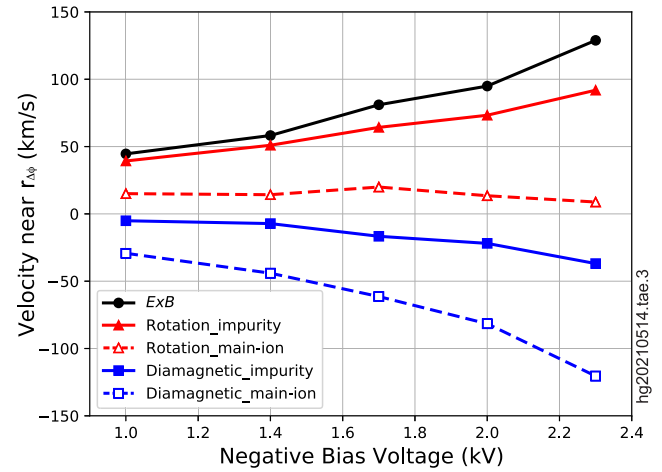


Figure 13. Measured $E \times B$ velocity ($v_{E \times B}$), toroidal ion rotation velocity ($v_{\theta i}$), and ion-diamagnetic velocity (v_{Di}) near FRC excluded-flux radius ($r_{\Delta\phi}$) as a function of negatively-applied bias voltage for O^{6+} impurity ions (solid lines) and main ions (dashed lines).

$r_{\Delta\phi}$, and a reduction of the normalized ion-scale density fluctuation level \tilde{n}/n (by 25%–30%) has indeed been observed at the higher electrode biasing voltage investigated here ($V_{\text{Bias}} \sim -2.3 \text{ kV}$).

3.2.4. Bayesian plasma reconstruction. Through collaboration with Google, a holistic high-fidelity plasma reconstruction based on Bayesian inference [60] has been developed and applied to study advanced beam-driven FRC plasmas in C-2W [61]. The method employs a statistical distribution of possible plasma states, including variables that persist across time points to enhance resolution of plasma dynamics. The time domain is split into 40–200 μs long ‘burst’ of frames separated by 2 μs ; the time-dependent state is reconstructed within each burst and the results are then stitched together. Within each burst, plasma is parameterized as an equilibrium shape, perturbed with rotating toroidal modes. This implementation of ‘time-linked’ Bayesian inference is used to evaluate density fluctuations at the C-2W midplane. Likely values and statistical confidence intervals are generated for density perturbation mode amplitudes, frequencies, and radial profiles. Synthesis of multiple high-frequency diagnostics (e.g. using FIR interferometer, Mirnov probe arrays, and SEE detectors) provides significantly increased reconstruction fidelity as compared to single instrument analysis. Figure 14 shows an example of reconstructed density profile, where plasma structure and displacement can be visually investigated and toroidal modes are analyzed. Recently, we have enhanced this plasma shape evolution reconstruction by supporting spiral structure modes, and allowing the radial mode profiles, amplitudes and frequencies (for toroidal modes $n = 1\text{--}4$) to slowly drift within the ‘burst’. These resulted in a better fit of the model to the measured data and allowed us to extend the burst duration to as long as 100 frames, covering 200 μs of plasma evolution. Compared to 20 frames per burst reported earlier [61], the 100 frames provided 5 times as much information, while the effective number of degrees of freedom of the model grew

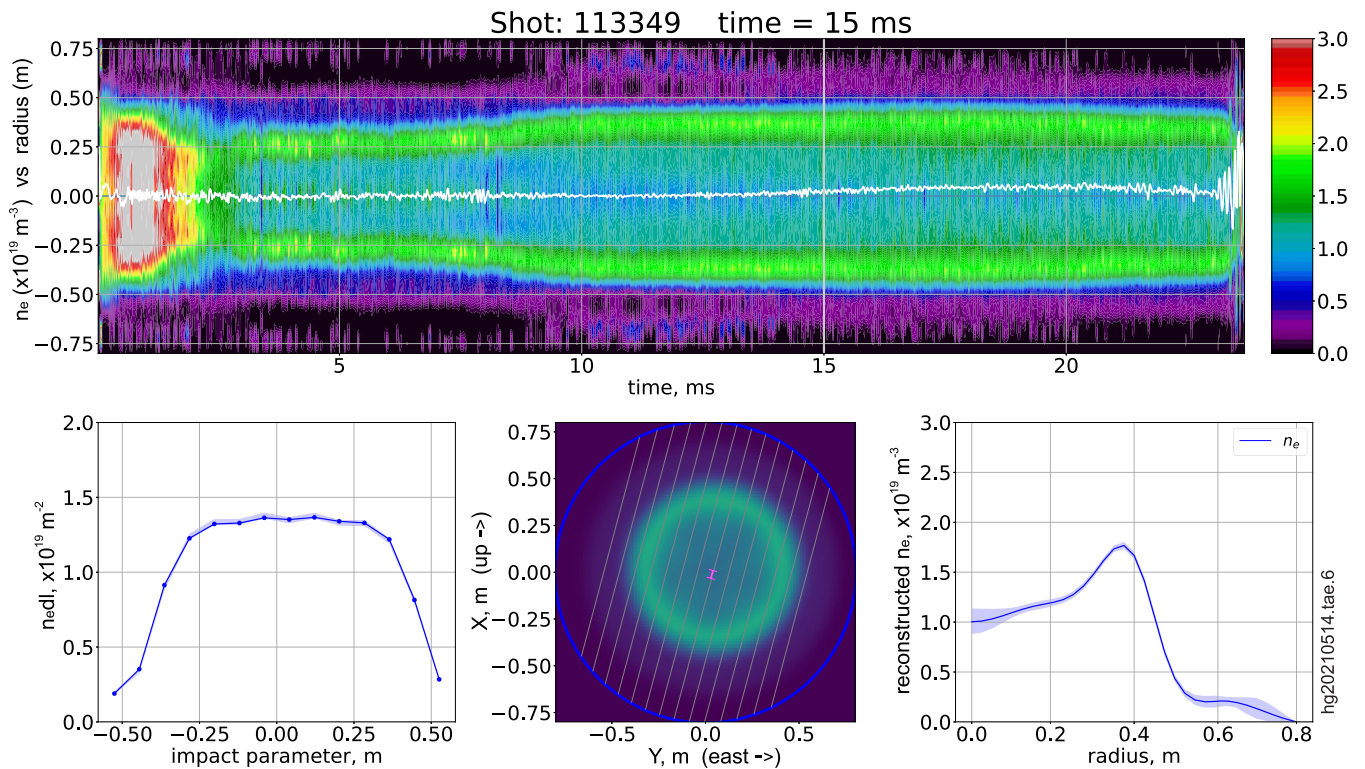


Figure 14. Example of reconstructed electron density profile evolution for shot 113 349 (top panel: density contour with a white line indicating reconstructed plasma radial displacement), with a single snapshot of the plasma state at $t \sim 15$ ms (bottom panels: left—line-integrated electron density measured by FIR interferometer; middle—reconstructed density in x - y plane with 14 chords of interferometer overlaid; right—radial profile of the reconstructed density, with blue shade showing 68% confidence interval).

only modestly. Increased amount of data per effective model degree of freedom gave an additional boost to the sensitivity of the method, which now allows to analyze vibration modes as small as 1%–2% of amplitude. The efficiency and robustness of this sampling technique has also been improved by using a series of heterogeneous preconditioners and adding a systematic quality control to the Hamiltonian Monte Carlo (HMC) at the core of our Bayesian inversion method. Details of this plasma reconstruction method and the enhancements to the preconditioned HMC are described in references [62, 63], respectively.

As an example, figure 15 shows an application of this reconstruction method to a neutral-beam termination experiment in C-2W. Amplitudes of toroidal modes $n = 1$ –4 and total NB input power as a function of time are shown, where 4 out of 8 NBs are turned off at $t \sim 18$ ms (at FRC equilibrium/quiescent phase). The injected and circulating large-orbit fast ions (figure 3) are known to macroscopically stabilize FRC plasma, working synergistically with edge biasing [14, 52, 53, 64]. One can see in figure 15 that in a few milliseconds after the beam termination, which is a typical lifetime of the fast ions, all modes start to grow, demonstrating the stabilization effect of the NBI. Based on the radial dependence of the modes, it is also found that the fluctuations are mostly concentrated near the outer edge of the FRC plasma, where the density gradient is the strongest. More details on the analysis can be found in reference [62].

3.2.5. Active control on FRC axial instability. Historically, there has been three important FRC parameters to discuss stability: (a) elongation, $E = l_s/(2r_s)$ (half of the ratio of the separatrix length l_s to the separatrix radius r_s); (b) normalized separatrix radius, $X_s = r_s/r_w$ (r_w : the wall radius); (c) kinetic parameter, $S^* = r_s/(c/\omega_{pi})$, (the ratio of the separatrix radius to the ion skin depth) [2, 3]. The plasma pressure profile and the separatrix beta have weaker effects on stability. The achievable parameter range depends on specifics of FRC formation method, external field shaping, and most importantly on global stability. The FRC is susceptible to tilt because the FRC magnetic moment is opposite to the external field, so that tilting reduces the total magnetic energy. Ideal MHD instability is muted by kinetic effects primarily finite-Larmor radius (FLR) and two-fluid effects [3, 65]. Both lead to a ‘stability’ condition where the tilt growth rate is greatly reduced if S^*/E is less than about three (for FLR effects theory), and it has also been found empirically that keeping the ratio $S^*/E < 3$ prevents the FRC plasma from tilting [3], in particular with NBI [10, 52].

In order to overcome the S^*/E plasma density limit, FRC plasma needs to be elongated to keep the ratio low enough for the stability threshold. In C-2W magnet systems can flexibly and adequately control the external magnetic field profile to modify the shape of FRC as well as fast-ion distributions. For instance, FRC plasma can be elongated by increasing the central magnetic field near the midplane; however, this makes

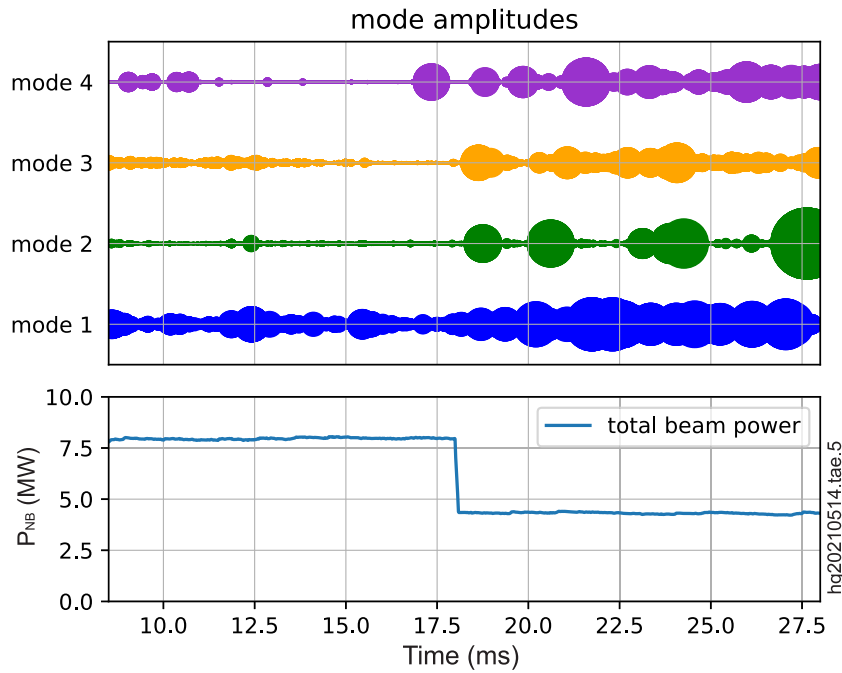


Figure 15. An example of instability (toroidal mode) growth due to reduced NBI power in the middle of FRC discharge at $t \sim 18$ ms (shot 119 549, at quiescent phase), indicative of insufficient stabilization effect from the reduced NBI. Relative mode amplitudes for $n = 1-4$ are depicted as a thickness/height of each band.

the plasma axially unstable due to the modified magnetic-field profile. One can imagine that FRC tends to shift axially to find and settle down in the minimum- B region of the confinement section. In this case, the FRC axial instability can be controlled by applying radial magnetic field as a function of the plasma axial position. Figure 16 shows an example of FRC axial instability with and without active control system enabled during the discharge, in which Trim magnets are regulated after $t \sim 13$ ms as illustrated by the shaded area in the figure. To create the radial field, the currents of Trim coils in north and south sides have the same intensity but opposite sign. As can be seen clearly in the figure, FRC axial instability leads to a short plasma lifetime without active control, but it is well stabilized by the active control system enabled. Due to the trim-current regulation, FRC moves axially back-and-forth but stays in the middle of the confinement section within ± 5 cm until the end of the shot (up to ~ 30 ms).

3.3. High temperature and energy state

3.3.1. High temperature regime. Adequately controlled external magnetic-field profile throughout the machine with a proper gas fueling has led to more effective edge biasing from the end-on plasma guns and electrodes in the outer divertors to globally stabilize plasma; thus, improving the efficiency of the NB-to-FRC coupling so that more plasma heating and current drive are obtained. Due to this synergistic effect of combining effective edge biasing and NBI on C-2W, FRC plasma state has further advanced to a higher temperature regime as shown in figure 17. Three different levels of electron temperature regimes are plotted in the figure (measured by the midplane Thomson scattering system [34]), where the temperature profiles of those 3 shots (#113301 in blue, #116474 in orange,

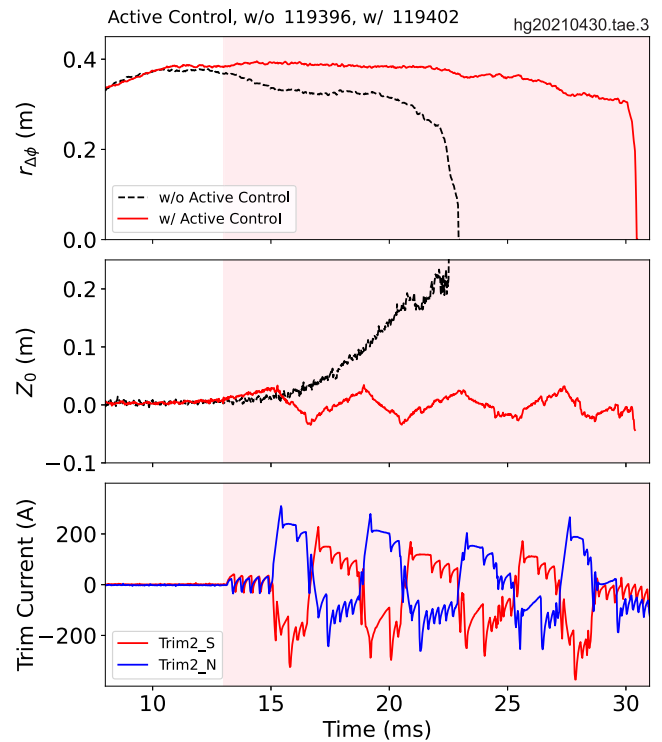


Figure 16. Actively controlled FRC axial position (Z_0) using trim coils during the discharge, where the shaded area indicates the real-time control system enabled. Only 2 out of 8 trim currents are shown for simplicity.

and #118340 in green at an equilibrium/quiescent phase) are largely flat in the FRC core region at the average T_e of ~ 200 , ~ 350 , and ~ 500 eV, respectively. A hollow density

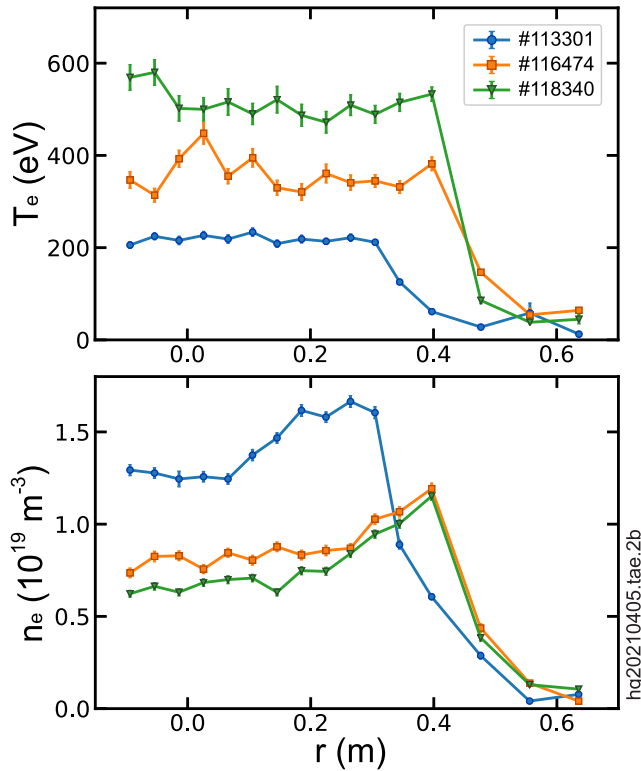


Figure 17. Electron temperature and density profiles of 3 shots at a quiescent phase, measured by the midplane Thomson scattering system.

profile is also observed and its peak is located just inside the excluded-flux radius of FRC, which is consistent with FIR interferometer density measurement as seen in figures 10 and 14. C-2W now can operate a wide range of temperature and density regimes. Furthermore, under the optimum operating condition, C-2W can produce $T_e > 500$ eV and total temperature $T_{\text{tot}} > 3$ keV. It is also important to note that a high electron pressure is obtained in more recent shots, as can be seen as an example by comparing shots 116474 and 118340 in figure 17; about 40% higher temperature in shot 118340 is observed while keeping almost the same density level as in shot 116474. This necessitates a higher external magnetic field operation to maintain the FRC plasma radius inside the CV wall as the internal plasma pressure grows.

3.3.2. Equilibrium reconstruction. To illustrate this high temperature FRC regime more systematically, figure 18 shows C-2W shot ensemble of the peak total temperature estimated from plasma equilibrium reconstruction as a function of the measured peak electron temperature from the midplane Thomson scattering system. TAE has developed an interpretative equilibrium reconstruction code [66] to calculate the internal magnetic field profile by solving Ampere's law in the paraxial limit, given as

$$\frac{\partial B_z}{\partial r} = \mu_0(J_p + J_f) = \frac{\mu_0}{en_e B_z} \left(\frac{\partial p_e}{\partial r} + \frac{n_e}{Z_i n_i} \frac{\partial p_i}{\partial r} \right) + \mu_0 J_f. \quad (2)$$

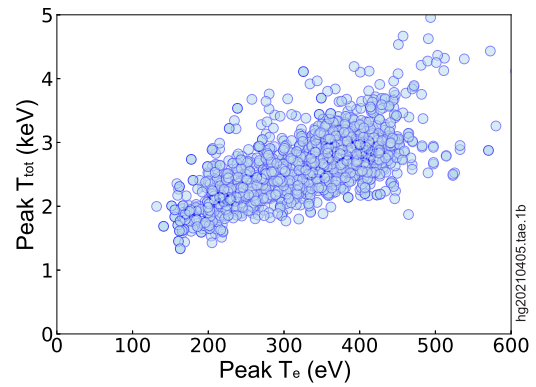


Figure 18. Peak total temperature (estimated from interpretative plasma reconstruction) as a function of peak T_e (measured by Thomson scattering) for ensembled C-2W shots at a quiescent phase.

The background diamagnetic plasma current density (J_p) is calculated using the experimentally measured electron density and temperature profiles. Fast-ion density (n_f) and current density (J_f) due to neutral-beam ions are calculated using kinetic Monte Carlo code in the presence of experimentally observed plasma profiles. The schematic of the iterative solver is shown in figure 19. The iterative/interpretative solver is initialized with the vacuum magnetic field and no fast ions. The background ions density and hence ion diamagnetic current is updated using the quasi-neutrality condition $n_i = n_e - n_f$ with increasing fast-ion population. Magnetic field is updated by solving Ampere's law (equation (2)). In the updated state, fast-ion density and current density are calculated by solving kinetic orbits with sources and losses. This iteration process continues with increasing fast-ion population until the magnetic flux, $\psi_w = \int_0^{r_w} B_z r dr$, converges to the experimentally measured magnetic flux near the CV wall. The contribution from the fast particles is controlled by changing the fast-ion losses due to charge exchange process. In this way, numerical analysis evolves from the low- β mirror plasma with no fast-ion current to high- β mirror plasma and finally to field-reversed plasmas, thus FRC magnetic structure.

For C-2W plasma parameters, the final converged state has field-reversed magnetic field and the profiles of fast-ion pressure, plasma pressure and magnetic pressure is shown in figure 20. It clearly shows the dominance of fast-ion pressure, much more than the background plasma pressure. Due to large fast-ion orbits and turning points well outside the FRC separatrix (figure 3), the fast-ion pressure may be an order of magnitude more than the plasma pressure. This total pressure analysis also provides the estimate of total temperature ($T_{\text{total}} = P_{\text{total}}/n_e$; for profile and peak value), as shown in figure 18, indicating that C-2W FRCs are exceeding 3 keV. Result of this total temperature estimate is consistent with experimentally measured T_{tot} based on pressure balance analysis [2], indicating higher T_{tot} as T_e increases.

3.3.3. High energy regime. FRC performance is well correlated with both NBI and edge biasing in C-2W. Figure 21

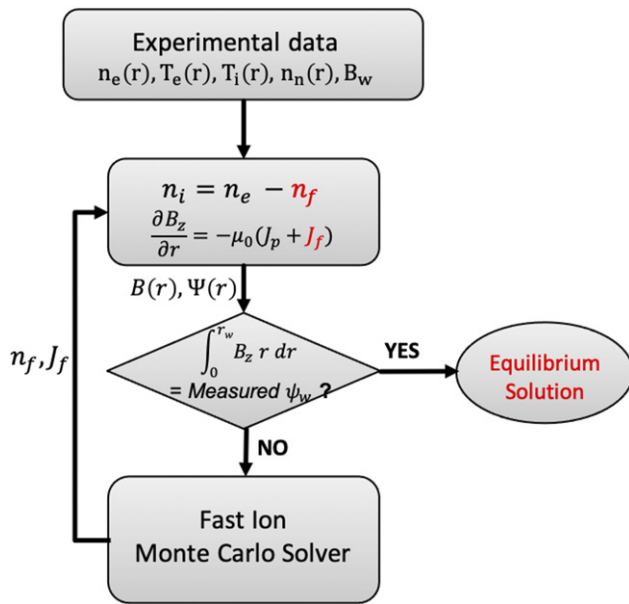


Figure 19. Schematic of the interpretative equilibrium reconstruction solver.

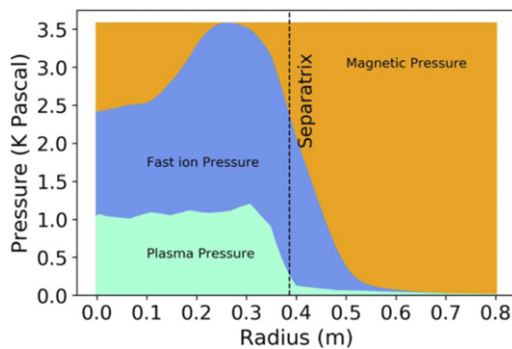


Figure 20. Profiles of magnetic pressure (orange), thermal plasma pressure (green) and fast-ion pressure (blue), showing the dominance of fast-ion pressure inside FRC separatrix for shot 113 301.

shows plasma total energy E_{tot} as functions of NB's input power and edge-biasing electrode voltage. As can be clearly seen, higher E_{tot} is obtained with higher NBI power and biasing voltage, indicating the importance of those systems to produce a good FRC plasma discharge. The total energy E_{tot} is estimated by integration of one-dimensional pressure reconstruction along the geometrical axis (z -axis). The 1D reconstruction corresponds to paraxial approximation (strongly elongated plasma) with the assumption of sharp boundary between plasma and surrounding magnetic field. The assumption of sharp boundary is the same as assumption which is used in the definition of excluded-flux radius [2]. By the way of E_{tot} is defined, it measures only perpendicular energy. Therefore, to compensate for that, E_{tot} uses coefficient 3/2 to include energy in the axial degree of freedom. A similar statistical analysis for FRC plasma thermal energy (E_{th}) has

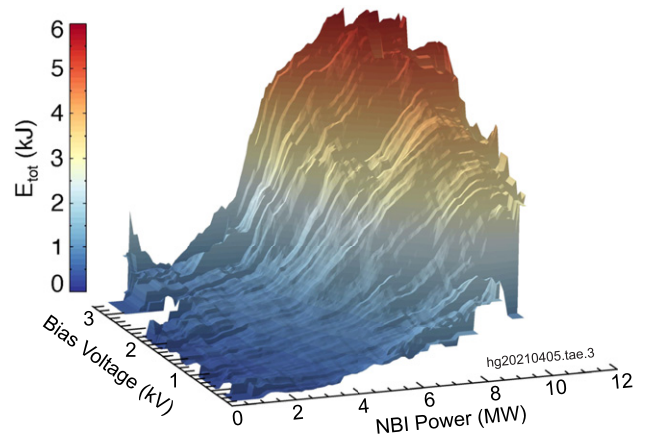


Figure 21. Plasma total energy as functions of NBI power and edge-biasing electrode voltage for ensembled C-2W shots at a quiescent phase.

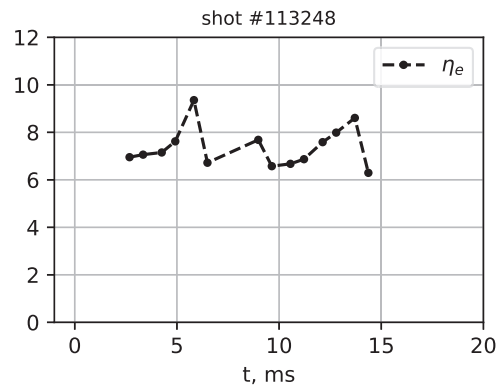


Figure 22. Energy lost per electron ion pair, η_e , measured at the end electrodes inside the outer divertors for shot 113 248.

also been done, and the result shows very similar trend and characteristics as seen in figure 21.

3.3.4. Reduced axial plasma losses in divertors. C-2W divertors are designed to achieve good electron heat confinement on open-field-lines using strong magnetic mirror fields as well as expanding the magnetic field in the divertors (expansion ratio >30); the concept is similar to the GDT divertors [20, 67]. To measure and characterize the open-field-line plasma outflow, C-2W is instrumented with a set of bolometers and electrostatic ion energy analyzers mounted on the end electrodes inside the outer divertors [47]. From these measurements one can determine the energy lost per electron ion pair, $\eta_e = P_e / (J_{\text{ion}} \cdot T_e)$. This parameter characterizes parallel electron heat confinement and is equal to 5–6 for the ideal case, but could be as large as $\sqrt{m_i/m_e} \sim 50$ if cold electron sources at the plasma edge degrade electrostatic confinement (like free-streaming electron losses). $\eta_e = (P_{\text{Tot}} - P_{\text{ion,thermal}}) / (T_e \times J_{\text{ion}})$ is calculated from the total power density of particle outflow measured by pyrobolometers, P_{Tot} , and the ion thermal outflow power, $P_{\text{ion,thermal}}$, and ion current density, J_{ion} , measured by the ion energy analyzers. Figure 22

shows experimental results of the measurement, indicating a value of $\eta_e \sim 6-8$ which is close to the ideal theoretical minimum. Measurements from a similar set of sensors on C-2U, which did not have extensive divertor pumping like C-2W to control cold electron sources, showed a much larger $\eta_e \sim 30$. In C-2W, it is also found that a strong ambipolar potential, $\sim 4-5 T_e$, develops along the open-field-lines to control electron losses [68].

This overall performance improvement in the open-field-line plasmas may corroborate the recent advancement in the high-temperature beam-driven FRC operations in C-2W. The previously-reported favorable energy confinement scaling [12, 21] is currently being updated to incorporate more accurate model of energy flow (e.g. power input/source and loss terms) into the global power-balance analysis. The newly-obtained high-temperature FRC regime is planned to be analyzed and reported elsewhere in the future [69].

4. Summary

The C-2W device is now reliably operational, producing stable, high temperature ($T_e > 500$ eV, $T_{tot} > 3$ keV), steady-state beam-driven FRCs up to 30 ms (limited by NB pulse length). Google's advanced optometrist algorithm and in-house active plasma control systems are routinely used in C-2W to produce superior FRC performance as well as for reliable machine operations. FRC performance is well correlated with NBs and edge-biasing system, where higher total plasma energy is obtained by increasing both NBI power and electrode-biasing voltage. C-2W divertors with strong magnetic mirror fields have demonstrated a good electron heat confinement on open-field-lines, achieving the energy lost per electron ion pair, $\eta_e \sim 6-8$, which is close to the ideal theoretical minimum.

Acknowledgments

The authors wish to thank the entire TAE Team for their dedicated work and effort to the C-2W program, Budker Institute colleagues for many key contributions to our experiments including studies of open-field-line plasmas and divertor physics as well as the key neutral beam development (for both heating NBs and diagnostic NB) and operations, Google research for their dedicated contributions to C-2W experiments such as sophisticated plasma optimizations and reconstruction using their extensive computational resources, as well as TAE's shareholders who made this exciting research effort possible.

ORCID iDs

H. Gota  <https://orcid.org/0000-0001-6475-2912>
M.W. Binderbauer  <https://orcid.org/0000-0002-2698-4744>
S.A. Dettrick  <https://orcid.org/0000-0002-1756-4625>
D.K. Gupta  <https://orcid.org/0000-0003-4849-1198>
S. Korepanov  <https://orcid.org/0000-0002-6118-729X>
R.M. Magee  <https://orcid.org/0000-0001-6697-7891>
T. Roche  <https://orcid.org/0000-0003-0840-4731>
J.A. Romero  <https://orcid.org/0000-0001-7585-1350>
E. Trask  <https://orcid.org/0000-0003-4984-6579>
K. Zhai  <https://orcid.org/0000-0002-8432-3696>
T. DeHaas  <https://orcid.org/0000-0003-3822-2074>
M.E. Griswold  <https://orcid.org/0000-0002-3922-295X>
S. Gupta  <https://orcid.org/0000-0001-5688-4122>
I. Allfrey  <https://orcid.org/0000-0001-8031-5384>
M. Beall  <https://orcid.org/0000-0002-5070-6824>
N.G. Bolte  <https://orcid.org/0000-0002-3702-4650>
A. Bondarenko  <https://orcid.org/0000-0003-0599-4721>
F. Ceccherini  <https://orcid.org/0000-0003-3377-6932>
C. Deng  <https://orcid.org/0000-0003-1092-9959>
C. Finucane  <https://orcid.org/0000-0003-4534-0001>
L. Galeotti  <https://orcid.org/0000-0003-3426-2087>
S. Galkin  <https://orcid.org/0000-0002-1670-7364>
E.M. Granstedt  <https://orcid.org/0000-0002-7691-4883>
M. Kaur  <https://orcid.org/0000-0001-6008-6676>
C.K. Lau  <https://orcid.org/0000-0001-6702-1461>
D. Marshall  <https://orcid.org/0000-0002-2062-0640>
R. Marshall  <https://orcid.org/0000-0003-0429-3923>
T. Matsumoto  <https://orcid.org/0000-0002-3217-3622>
R. Mendoza  <https://orcid.org/0000-0002-1761-6165>
L. Morton  <https://orcid.org/0000-0003-2401-2463>
M. Nations  <https://orcid.org/0000-0002-7795-1555>
S. Nicks  <https://orcid.org/0000-0002-3876-8299>
M. Onofri  <https://orcid.org/0000-0003-0818-4628>
A. Ottaviano  <https://orcid.org/0000-0003-0255-3824>
E. Parke  <https://orcid.org/0000-0002-5765-8829>
K. Phung  <https://orcid.org/0000-0002-1732-172X>
T.M. Schindler  <https://orcid.org/0000-0002-6856-1707>
R.J. Smith  <https://orcid.org/0000-0002-3595-781X>
V. Sokolov  <https://orcid.org/0000-0003-4971-033X>
L.C. Steinhauer  <https://orcid.org/0000-0003-2227-7345>
J.B. Titus  <https://orcid.org/0000-0002-6457-3751>
A. Tkachev  <https://orcid.org/0000-0002-5180-0548>
A.D. Van Drie  <https://orcid.org/0000-0002-6776-9688>
L. Schmitz  <https://orcid.org/0000-0003-1346-0914>
Z. Lin  <https://orcid.org/0000-0003-2007-8983>
T. Asai  <https://orcid.org/0000-0001-9440-0117>
E.A. Baltz  <https://orcid.org/0000-0002-4827-1542>
M. Dikovskiy  <https://orcid.org/0000-0002-3246-4040>
A. Kast  <https://orcid.org/0000-0002-0755-9996>
J.C. Platt  <https://orcid.org/0000-0002-5652-5303>

References

- [1] Details on TAE Technologies website at (<https://tae.com>)
- [2] Tuszewski M. 1988 Field reversed configurations *Nucl. Fusion* **28** 2033
- [3] Steinhauer L.C. 2011 Review of field-reversed configurations *Phys. Plasmas* **18** 070501
- [4] Luce T.C. 2011 Realizing steady-state tokamak operation for fusion energy *Phys. Plasmas* **18** 030501
- [5] Beidler C.D. *et al* 2002 Stellarator fusion reactors—an overview *J. Plasma Fusion Res.* **5** 149
- [6] Rostoker N. *et al* 1997 Colliding beam fusion reactor *Science* **278** 1419
- [7] Putvinski S.V., Ryutov D.D. and Yushmanov P.N. 2019 Fusion reactivity of the pB¹¹ plasma revisited *Nucl. Fusion* **59** 076018
- [8] Gota H. *et al* 2019 Formation of hot, stable, long-lived field-reversed configuration plasmas on the C-2W device *Nucl. Fusion* **59** 112009
- [9] Binderbauer M.W. *et al* 2010 Dynamic formation of a hot field reversed configuration with improved confinement by super-sonic merging of two colliding high- β compact toroids *Phys. Rev. Lett.* **105** 045003
- [10] Binderbauer M.W. *et al* 2015 A high performance field-reversed configuration *Phys. Plasmas* **22** 056110
- [11] Binderbauer M.W. *et al* 2016 Recent breakthroughs on C-2U: Norman's legacy *AIP Conf. Proc.* **1721** 030003
- [12] Gota H. *et al* 2017 Achievement of field-reversed configuration plasma sustainment via 10 MW neutral-beam injection on the C-2U device *Nucl. Fusion* **57** 116021
- [13] Guo H.Y. *et al* 2011 Formation of a long-lived hot field reversed configuration by dynamically merging two colliding high- β compact toroids *Phys. Plasmas* **18** 056110
- [14] Tuszewski M. *et al* 2012 Field reversed configuration confinement enhancement through edge biasing and neutral beam injection *Phys. Rev. Lett.* **108** 255008
- [15] Dunaevsky A. *et al* 2018 Neutral beam injection system with tunable beam energy for the C-2W experiment *Bull. Am. Phys. Soc.* **TO6** 00015
- [16] Sokolov V. *et al* 2019 Electrode biasing system in C-2W *Bull. Am. Phys. Soc.* **UP10** 00141
- [17] Romero J.A. *et al* 2019 The C-2W plasma control system: overview and experimental results *Bull. Am. Phys. Soc.* **UP10** 00127
- [18] Thompson M.C., Schindler T.M., Mendoza R., Gota H., Putvinski S. and Binderbauer M.W. 2018 Integrated diagnostic and data analysis system of the C-2W advanced beam-driven field-reversed configuration plasma experiment *Rev. Sci. Instrum.* **89** 10K114
- [19] Roche T., Romero J., Zhai K., Granstedt E., Gota H., Putvinski S., Smirnov A. and Binderbauer M.W. 2021 The integrated diagnostic suite of the C-2W experimental field-reversed configuration device and its applications *Rev. Sci. Instrum.* **92** 033548
- [20] Ivanov A.A. and Prikhodko V.V. 2013 Gas-dynamic trap: an overview of the concept and experimental results *Plasma Phys. Control. Fusion* **55** 063001
- [21] Trask E. *et al* 2016 C-2U experimental transport analysis *Bull. Am. Phys. Soc.* **CP10** 00064
- [22] Baltz E.A., Trask E., Binderbauer M., Dikovsky M., Gota H., Mendoza R., Platt J.C. and Riley P.F. 2017 Achievement of sustained net plasma heating in a fusion experiment with the optometrist algorithm *Sci. Rep.* **7** 6425
- [23] Galeotti L., Barnes D.C., Ceccherini F. and Pegoraro F. 2011 Plasma equilibria with multiple ion species: equations and algorithm *Phys. Plasmas* **18** 082509
- [24] Bolte N., Allfrey I. and Mendoza R. 2021 Automated signal classification in the C-2W fusion experiment *Rev. Sci. Instrum.* **92** 053502
- [25] Deichuli P., Davydenko V., Ivanov A., Korepanov S., Mishagin V., Smirnov A., Sorokin A. and Stupishin N. 2015 Low energy, high power hydrogen neutral beam for plasma heating *Rev. Sci. Instrum.* **86** 113509
- [26] Matsumoto T. *et al* 2016 Development of a magnetized coaxial plasma gun for compact toroid injection into the C-2 field-reversed configuration device *Rev. Sci. Instrum.* **87** 053512
- [27] Asai T. *et al* 2017 Compact toroid injection fueling in a large field-reversed configuration *Nucl. Fusion* **57** 076018
- [28] Vinyer I.V. *et al* 2014 A 12-barrel deuterium pellet injector for the C-2 field-reversed configuration device *Instrum. Exp. Tech.* **57** 508
- [29] Roche T., Thompson M.C., Griswold M., Knapp K., Koop B., Ottaviano A., Tobin M., Magee R. and Matsumoto T. 2018 Magnetic diagnostic suite of the C-2W field-reversed configuration experiment *Rev. Sci. Instrum.* **89** 10J107
- [30] Deng B.H. *et al* 2018 Development of a three-wave far-infrared laser interferometry and polarimetry diagnostics for the C-2W FRC experiment *Rev. Sci. Instrum.* **89** 10B109
- [31] Smith R.J. 2018 A combined millimeter wave and CO₂ interferometer on the C-2W Jet plasma *Rev. Sci. Instrum.* **89** 10B110
- [32] Brandi F., Giammanco F., Harris W.S., Roche T., Trask E. and Wessel F.J. 2009 Electron density measurements of a field-reversed configuration plasma using a novel compact ultra-stable second-harmonic interferometer *Rev. Sci. Instrum.* **80** 113501
- [33] Sheftman D., Schmitz L., Gupta D. and Thompson M.C. 2018 Jet outflow and open field line measurements on the C-2W advanced beam-driven field-reversed configuration plasma experiment *Rev. Sci. Instrum.* **89** 10D120
- [34] Zhai K., Schindler T., Ottaviano A., Zhang H., Fallah D., Wells J., Parke E. and Thompson M.C. 2018 Thomson scattering systems on C-2W field-reversed configuration plasma experiment *Rev. Sci. Instrum.* **89** 10C118
- [35] Ottaviano A., Schindler T.M., Zhai K., Parke E., Granstedt E. and Thompson M.C. 2018 Characterization and calibration of the Thomson scattering diagnostic suite for the C-2W field-reversed configuration experiment *Rev. Sci. Instrum.* **89** 10C120
- [36] Nations M., Gupta D., Sweeney J., Frausto L. and Tobin M. 2021 Measurements of impurity ion temperature and velocity distributions via active charge-exchange recombination spectroscopy in C-2W *Rev. Sci. Instrum.* **92** 053512
- [37] Gupta D.K., Nations M., Sweeney J., Aviles J., Leinweber H. and Marshall R.S. 2021 Main-ion charge exchange recombination spectroscopy on C-2W FRC plasmas *Rev. Sci. Instrum.* **92** 073508
- [38] Schmitz L., Deng B., Thompson M., Gota H., Lau C., Fulton D.P., Lin Z., Tajima T. and Binderbauer M. 2018 Combination Doppler backscattering/cross-polarization scattering diagnostic for the C-2W field-reversed configuration *Rev. Sci. Instrum.* **89** 10H116
- [39] Bolte N.G., Nations M., Gupta D. and Aviles J. 2018 Fast-ion D-alpha diagnostic development for the C-2W field-reversed configuration plasma *Rev. Sci. Instrum.* **89** 10D106
- [40] Granstedt E.M., Gupta D., Sweeney J., Tobin M. and Dikovsky M. 2021 Comprehensive imaging of C-2W plasmas: Instruments and applications *Rev. Sci. Instrum.* **92** 043515
- [41] Osin D. and Schindler T. 2016 Dual wavelength imaging of a scrape-off layer in an advanced beam-driven field-reversed configuration *Rev. Sci. Instrum.* **87** 11E514

- [42] Nations M., Gupta D., Bolte N. and Thompson M.C. 2018 Development of a Z_{eff} diagnostic using visible and near-infrared bremsstrahlung light for the C-2W field-reversed configuration plasma *Rev. Sci. Instrum.* **89** 10D130
- [43] Titus J.B., Korepanov S., Tkachev A., Pirogov K. and Knapp K. 2021 Wire calorimeter for direct neutral beam power measurements on C-2W *Rev. Sci. Instrum.* **92** 053520
- [44] Titus J.B., Magee R.M., Isakov I., Pirogov K. and Korepanov S. 2018 Secondary electron emission detectors for neutral beam characterization on C-2W *Rev. Sci. Instrum.* **89** 10I123
- [45] Roche T., Sun X., Armstrong S., Knapp K. and Slepchenkov M. 2014 Langmuir probe diagnostic suite in the C-2 field-reversed configuration *Rev. Sci. Instrum.* **85** 11D824
- [46] Dubois A.M., Sokolov V., Knapp K. and Thompson M.C. 2018 Design of a custom insertable probe platform for measurements of C-2W inner divertor plasma parameters *Rev. Sci. Instrum.* **89** 10J115
- [47] Griswold M.E., Granstedt E.M., Thompson M.C., Knapp K. and Koop B. 2018 Particle and heat flux diagnostics on the C-2W divertor electrodes *Rev. Sci. Instrum.* **89** 10J110
- [48] Magee R.M., Clary R., Korepanov S., Jauregui F., Allfrey I., Garate E., Valentine T. and Smirnov A. 2016 Absolute calibration of neutron detectors on the C-2U advanced beam-driven FRC *Rev. Sci. Instrum.* **87** 11D815
- [49] Clary R., Roquemore A., Douglass J., Jaramillo D., Korepanov S., Magee R., Medley S. and Smirnov A. 2016 A mass resolved, high resolution neutral particle analyzer for C-2U *Rev. Sci. Instrum.* **87** 11E703
- [50] Magee R.M., Clary R., Korepanov S., Smirnov A., Garate E., Knapp K. and Tkachev A. 2014 Fusion proton diagnostic for the C-2 field-reversed configuration *Rev. Sci. Instrum.* **85** 11D851
- [51] McCullagh P. and Nelder J.A. 1989 *Generalized Linear Models* 2nd edition (Boca Rato, FL: Chapman & Hall/CRC)
- [52] Guo H.Y. *et al* 2015 Achieving a long-lived high-beta plasma state by energetic beam injection *Nat. Commun.* **6** 6897
- [53] Schmitz L. *et al* 2016 Suppressed ion-scale turbulence in a hot high- β plasma *Nat. Commun.* **7** 13860
- [54] Tuszewski M., Gupta D., Gupta S., Onofri M., Osin D., Deng B.H., Dettrick S.A., Hubbard K. and Gota H. 2017 Equilibrium properties of hybrid field reserved configurations *Phys. Plasmas* **24** 012502
- [55] Tobin M., Roche T. and Matsumoto T. 2021 MHD mode identification by higher order singular value decomposition of C-2W Mirnov probe data *Rev. Sci. Instrum.* **92** 043510
- [56] Deng B.H. *et al* 2018 First experimental measurements of a new fast ion driven micro-burst instability in a field-reversed configuration plasma *Nucl. Fusion* **58** 126026
- [57] Magee R.M., Necas A., Clary R., Korepanov S., Nicks S., Roche T., Thompson M.C., Binderbauer M.W. and Tajima T. 2019 Direct observation of ion acceleration from a beam-driven wave in a magnetic fusion experiment *Nat. Phys.* **15** 281
- [58] Lau C.K., Fulton D.P., Holod I., Lin Z., Binderbauer M., Tajima T. and Schmitz L. 2017 Drift-wave stability in the field-reversed configuration *Phys. Plasmas* **24** 082512
- [59] Biglari H., Diamond P.H. and Terry P.W. 1990 Influence of sheared poloidal rotation on edge turbulence *Phys. Fluids B* **2** 1
- [60] Svensson J. and Werner A. 2007 Large scale Bayesian data analysis for nuclear fusion experiments *IEEE Int. Symp. Intelligent Signal Processing* (Alcala de Henares, Spain)
- [61] Norgaard P.C. *et al* 2019 High-fidelity Bayesian inference of transient FRC plasma perturbations in C-2W *Bull. Am. Phys. Soc.* **UP10** 00128
- [62] Dikovskiy M. *et al* 2021 Multi-instrument Bayesian reconstruction of plasma shape evolution in the C-2W experiment *Phys. Plasmas* **28** 062503
- [63] Langmore I. *et al* 2021 Hamiltonian Monte Carlo in inverse problems; ill-conditioning and multi-modality arXiv:2103.07515
- [64] Dettrick S.A. *et al* 2021 Simulation of equilibrium and transport in advanced FRCs *Nucl. Fusion* **61** (private communication)
- [65] Belova E.V., Davidson R.C., Ji H. and Yamada M. 2004 Kinetic effects on the stability properties of field-reversed configurations. II. Nonlinear evolution *Phys. Plasmas* **11** 2523
- [66] Gupta S. *et al* 2019 One-dimensional equilibrium of C-2W plasma *Bull. Am. Phys. Soc.* **UP10** 00149
- [67] Yakovlev D.V., Shalashov A.G., Gospodchikov E.D., Maximov V.V., Prikhodko V.V., Savkin V.Y., Soldatkina E.I., Solomakhin A.L. and Bagryansky P.A. 2018 Stable confinement of high-electron-temperature plasmas in the GDT experiment *Nucl. Fusion* **58** 094001
- [68] Griswold M.E. *et al* 2019 Measurement of axial plasma losses in the C-2W high performance regime *Bull. Am. Phys. Soc.* **UP10** 00140
- [69] Trask E., Schmitz L., Tajima T. *et al* 2021 *Positive-power temperature scaling of plasma energy confinement time in a beam-driven field-reversed configuration* (private communication)